The ALMA REBELS Survey. Epoch of Reionization giants: properties of dusty galaxies at $z \approx 7$

A. Ferrara [ID],[1] L. Sommovigo [ID],[1] P. Dayal [ID],[2] A. Pallottini [ID],[1] R.J. Bouwens [ID],[3] V. Gonzalez [ID],[4,5]
H. Inami [ID],[6] R. Smit [ID],[7] R.A.A. Bowler [ID],[8] R. Endsley [ID],[9] P. Oesch [ID],[10,11] S. Schouws [ID],[3] D. Stark,[9]
M. Stefanon [ID],[3] M. Aravena [ID],[12] E. da Cunha [ID],[13,14] I. De Looze [ID],[15,16] Y. Fudamoto [ID],[10,17,18]
L. Graziani [ID],[19,20] J. Hodge [ID],[3] D. Riechers [ID],[21] R. Schneider [ID],[19,22,23,24] H.S.B. Algera [ID],[6] L. Barrufet [ID],[10]
A.P.S. Hygate [ID],[3] I. Labbé [ID],[25] C. Li [ID],[26,27] T. Nanayakkara [ID],[25] M. Topping [ID],[9] and P. van der Werf [ID][3]

[1]Scuola Normale Superiore, Piazza dei Cavalieri 7, 50126 Pisa, Italy
[2]Kapteyn Astronomical Institute, University of Groningen, 9700 AV Groningen, The Netherlands
[3]Leiden Observatory, Leiden University, NL-2300 RA Leiden, Netherlands
[4]Departmento de Astronomia, Universidad de Chile, Casilla 36-D, Santiago 7591245, Chile
[5]Centro de Astrofisica y Tecnologias Afines (CATA), Camino del Observatorio 1515, Las Condes, Santiago, 7591245, Chile
[6]Hiroshima Astrophysical Science Center, Hiroshima University, 1-3-1 Kagamiyama, Higashi-Hiroshima, Hiroshima 739-8526, Japan
[7]Astrophysics Research Institute, Liverpool John Moores University, 146 Brownlow Hill, Liverpool L3 5RF, UK
[8]Astrophysics, The Denys Wilkinson Building, University of Oxford, Keble Road, Oxford, OX1 3RH, UK
[9]Steward Observatory, University of Arizona, 933 N Cherry Ave, Tucson, AZ 85721, USA
[10]Observatoire de Genève, 1290 Versoix, Switzerland
[11]Cosmic Dawn Center (DAWN), Niels Bohr Institute, University of Copenhagen, Jagtvej 128, København N, DK-2200, Denmark
[12]Nucleo de Astronomia, Facultad de Ingenieria y Ciencias, Universidad Diego Portales, Av. Ejercito 441, Santiago, Chile
[13]International Centre for Radio Astronomy Research, University of Western Australia, 35 Stirling Hwy, Crawley,26WA 6009, Australia
[14]ARC Centre of Excellence for All Sky Astrophysics in 3 Dimensions (ASTRO 3D), Australia
[15]Sterrenkundig Observatorium, Ghent University, Krijgslaan 281 - S9, 9000 Gent, Belgium
[16]Dept. of Physics & Astronomy, University College London, Gower Street, London WC1E 6BT, UK
[17]Research Institute for Science and Engineering, Waseda University, 3-4-1 Okubo, Shinjuku, Tokyo 169-8555, Japan
[18]National Astronomical Observatory of Japan, 2-21-1, Osawa, Mitaka, Tokyo, Japan
[19]Dipartimento di Fisica, Sapienza, Universitá di Roma, Piazzale Aldo Moro 5, I-00185 Roma, Italy
[20]INAF/Osservatorio Astrofisico di Arcetri, Largo E. Fermi 5, 50125 Firenze, Italy
[21]I. Physikalisches Institut, Universität zu Köln, Zülpicher Strasse 77, D-50937 Köln, Germany
[22]Sapienza School for Advanced Studies, Viale Regina Elena 291, 00161 Roma Italy
[23]INAF/Osservatorio Astronomico di Roma, via Frascati 33, 00078 Monte Porzio Catone, Roma, Italy
[24]Istituto Nazionale di Fisica Nucleare, Sezione di Roma1, Piazzale Aldo Moro 2, 00185 Roma Italy
[25]Centre for Astrophysics & Supercomputing, Swinburne University of Technology, PO Box 218, Hawthorn, VIC 3112, Australia
[26]Department of Astronomy & Astrophysics, The Pennsylvania State University, 525 Davey Lab, University Park, PA 16802, USA
[27]Institute for Gravitation and the Cosmos, The Pennsylvania State University, University Park, PA 16802, USA

ABSTRACT

We analyse FIR dust continuum measurements for 14 galaxies (redshift $z \approx 7$) in the ALMA REBELS Large Program to derive their physical properties. Our model uses three input data, i.e. (a) the UV spectral slope, β, (b) the observed UV continuum flux at 1500Å, F_{1500}, (c) the observed continuum flux at $\approx 158\mu$m, F_{158}, and considers Milky Way (MW) and SMC extinction curves, along with different dust geometries. We find that REBELS galaxies have $28 - 90.5\%$ of their star formation obscured; the *total* (UV+IR) star formation rates are in the range $31.5 < \mathrm{SFR}/(\mathrm{M}_\odot \mathrm{yr}^{-1}) < 129.5$. The sample-averaged dust mass and temperature are $(1.3 \pm 1.1) \times 10^7 M_\odot$ and 52 ± 11 K, respectively. However, in some galaxies dust is particularly abundant (REBELS-14, $M'_d \approx 3.4 \times 10^7 M_\odot$), or hot (REBELS-18,

Corresponding author: Andrea Ferrara
andrea.ferrara@sns.it

$T'_d \approx 67$ K). The dust distribution is compact (< 0.3 kpc for 70% of the galaxies). The inferred dust yield per supernova is $0.1 \leq y_d/M_\odot \leq 3.3$, with 70% of the galaxies requiring $y_d < 0.25 M_\odot$. Three galaxies (REBELS-12, 14, 39) require $y_d > 1 M_\odot$, which is likely inconsistent with pure SN production, and might require dust growth via accretion of heavy elements from the interstellar medium. With the SFR predicted by the model and a MW extinction curve, REBELS galaxies detected in [CII] nicely follow the local $L_{CII}-$SFR relation, and are approximately located on the Kennicutt-Schmidt relation. The sample-averaged gas depletion time is of $0.11\, y_P^{-2}$ Gyr, where y_P is the ratio of the gas-to-stellar distribution radius. For some systems a solution simultaneously matching the observed $(\beta, F_{1500}, F_{158})$ values cannot be found. This occurs when the index $I_m = (F_{158}/F_{1500})/(\beta - \beta_{int})$, where β_{int} is the intrinsic UV slope, exceeds $I_m^* \approx 1120$ for a MW curve. For these objects we argue that the FIR and UV emitting regions are not co-spatial, questioning the use of the IRX-β relation.

1. INTRODUCTION

Although many aspects of the process, such as e.g. the detailed time evolution, topology of ionized regions, ionizing (LyC) photons emissivity and their escape fraction from early galaxies, are still largely unknown, there is a large consensus (for a discussion, see Ciardi & Ferrara 2005; Wise 2019) that reionization was predominantly powered by photons emitted by stars within small galaxies in $10^{8-9} M_\odot$ dark matter halos (Choudhury et al. 2008; Mitra et al. 2015; Robertson et al. 2015).

Identifying the reionization sources with available instrumentation has represented one of the most intense areas of activity (reviewed in Dayal & Ferrara 2018) in observational cosmology in the last two decades. Such searches typically exploit two distinct techniques, fully described in e.g. Dunlop (2013), based on the detection of either (a) the 912Å Lyman break caused by the absorption of LyC photons by interstellar/intergalactic neutral gas[1], or (b) the prominent Lyα line emission. These two strategies yield separate (but likely overlapping, see Dayal & Ferrara 2012) samples of EoR galaxies known as Lyman Break Galaxies (LBG) and Lyman Alpha Emitters (LAE).

These combined efforts were amazingly successful, and they have allowed to build the UV and Lyα luminosity functions (LF) of EoR galaxies down to very faint magnitudes. For example, at $z \simeq 7$ the UV LF is now sampled over about 8 magnitudes in the range $-22.6 < M_{UV} < -14.5$ (Ono et al. 2018). These observations used a combination of space-born surveys using HST (Oesch et al. 2010; McLure et al. 2013; Bouwens et al. 2014), in some cases exploiting gravitational lensing of massive galaxy clusters, such as the Hubble Fron-

tier Fields (Lotz et al. 2017; Livermore et al. 2017; Ishigaki et al. 2018; Bhatawdekar & Conselice 2021) and other similar programs such as RELICS (Salmon et al. 2018), and ground telescopes (Bowler et al. 2015; Bouwens et al. 2016). A full description of the development in the field along with the theoretical implications can be found in Dayal & Ferrara (2018). A comprehensive review of the present knowledge of the LF up to $z = 9$ is given in Bouwens et al. (2021a); Oesch et al. (2018) and Bowler et al. (2020) obtained preliminary determinations at even earlier times (up to $z \approx 10$).

These studies have produced a better characterisation of the faint-end of the LF carrying information on the reionization sources. In addition, they have enabled the investigation of the EoR "giants", i.e. luminous, massive galaxies (Naidu et al. 2020; Trebitsch et al. 2020) shaping the bright end of the LF. Using the ULTRA-VISTA and VIDEO surveys, Bowler et al. (2020) found a steepening of the $z > 5$ LF bright-end slope over the $-23 < M_{UV} < -17$ range.

Indeed, if dust is present already at these very early cosmic epochs, its effects are expected to be more evident on the most massive galaxies. This is because to a first approximation, and for a fixed dust yield, the dust mass is expected to be proportional to the stellar mass.

The presence of sizeable amounts of dust has a strong impact on galaxy evolution. Dust governs the interstellar medium (ISM) thermal balance (Draine 2003; Galliano et al. 2018) by providing photoelectric heating, it controls important chemical processes such as the formation of H_2 (Tielens 2010), which in turn drives molecular chemistry. Thus, determining the dust content of EoR galaxies is crucial to interpret observations (Mancini et al. 2016; Behrens et al. 2018; Wilkins et al. 2018; Arata et al. 2019; Vogelsberger et al. 2020; Inoue et al. 2020; Di Mascia et al. 2021a,b; Shen et al. 2021), and build a coherent picture of early galaxy formation.

---

[1] More precisely, at $z > 4$, the Lyα forest becomes the dominant factor, and at $z > 6$ we observe a complete Lyα break.

Grains absorb the stellar UV light and re-radiate it in the infrared, shielding the dense gas, ultimately triggering the formation of molecular clouds where new stars are born. However, determining the mass content purely from UV observations is difficult (Calzetti 2001; Cortese et al. 2006). Combining UV and IR observations is then fundamental to constrain the dust content and, even more crucially, the optical and physical properties of the grains, such as their temperature, size distribution and composition (Draine 2003). In turn, such information holds the key to investigate the ISM of the first galaxies, and clarify the energy and mass exchange of these systems with the surrounding environment.

Last but not least, the origin and rapid cosmic evolution of dust is a long-standing question (Todini & Ferrara 2001; Ginolfi et al. 2018; Leśniewska & Michałowski 2019) that has received only partial answers.

Multi-wavelength observations of galaxies are routinely performed locally (see, e.g., Cormier et al. 2019), and have enabled mighty insights on the physical properties of these systems, and the processes regulating them, particularly for what concerns their ISM. This approach becomes increasingly challenging towards high redshift due to both the faintness of the sources, and the redshifting of diagnostic spectral features to electromagnetic bands out of reach of available instrumentation. With the advent of ALMA, which will soon followed by JWST, the situation has drastically improved.

In the last few years ALMA observations (Watson et al. 2015; Laporte et al. 2017; Hashimoto et al. 2019; Bakx et al. 2020; Faisst et al. 2020; Hodge & da Cunha 2020; Gruppioni et al. 2020; Schouws et al. 2021; Bakx et al. 2021) have detected dust thermal emission in "normal" galaxies[2] well into the EoR ($z \approx 7$). The copious IR continuum emission from these early galaxies came, at least partly, as a surprise. Naively, a common expectation was that these remote galaxies are low-metallicity, low-dust content systems, although some high-resolution simulations have suggested that enrichment could be very fast, particularly close to star forming regions (Behrens et al. 2018; Wilkins et al. 2018; Pallottini et al. 2019; Graziani et al. 2020).

The dust mass of detected EoR galaxies remains nevertheless uncertain, due to the degeneracy with dust temperature; estimates are in the range $10^{6-8} M_\odot$. Interestingly, a quasi-linear, global redshift evolution of the dust temperature is suggested by some studies (Magdis et al. 2012; Schreiber et al. 2018; Bethermin

et al. 2020; Faisst et al. 2020). However, the errors in the existing data are large and do not allow to draw firm conclusions yet[3]. A statistically significant sample of EoR galaxies is a precondition to assess the existence and physical nature of the relation.

In this context, the ALMA Reionization Era Bright Emission Line Survey (REBELS) Large Program (Bouwens et al. 2021b) provides a unique sample of the most massive star-forming galaxies at $z > 6.5$. REBELS targets 40 of the brightest (and most robust) galaxies identified over a 7 deg^2 area of the sky, and systematically scanning these galaxies for bright ISM-cooling lines (such as the [CII] 158μm and [OIII] 88μm) and dust-continuum emission. In the first paper from the collaboration, Fudamoto et al. (2021) reported the discovery of two dust-obscured star-forming galaxies at $z = 6.6813 \pm 0.0005$ and $z = 7.3521 \pm 0.0005$. These objects are not detected in existing rest-frame UV data and were discovered only through their [CII] line and dust continuum emission as companions to typical UV-luminous galaxies at the same redshift.

The goal of this paper is to use the newly acquired REBELS data in combination with pre-existing UV data to infer the physical properties of these early systems in a self-consistent manner. Such data are partially already presented in Bouwens et al. (2021b), but more details will be given in Schouws et al. 2022, in prep.; Inami et al. 2022, in prep.; Stefanon et al. 2022, in prep.

In addition to their dust content and temperature, this study also aims at determining the obscured star formation fraction, and constraining the dust yields from the major dust factories in the EoR, i.e. supernovae. In two companion theoretical papers of the REBELS Collaboration, we discuss the implications for the UV luminosity function (Dayal et al. 2022, in prep.), and dust temperature redshift evolution (Sommovigo et al. 2022, in prep).

The plan of the paper is as follows. In Sec. 2 we describe the method to derive the relevant physical galaxy quantities from UV and FIR data. The results are presented in Sec. 3, and their additional implications discussed in Sec. 4. Sec. 5 contains a discussion on the use of the IRX-β relations and the multi-phase nature of some of the REBELS galaxies. Finally, a brief summary is provided in Sec. 6. For consistency with the data analysis, we adopt the following cosmological parameters: $\Omega_m = 0.3, \Omega_\Lambda = 0.7, h = 0.7$.

2. METHOD

---

[2] We recall that the presence of dust at $z > 6$ was already ascertained from observations of quasar hosts and massive dusty starbursts; for a review see, e.g. Casey et al. (2014)

[3] Similar uncertainties hold also for sub-millimeter galaxies, Dudzevičiūtė et al. (see, e.g. 2020)

In this Section we describe the analytical method used to derive the properties of the sample galaxies from the REBELS data. It consists of several steps, each of which is detailed in the following subsections.

The method uses as an input three quantities (in addition to the source redshift z_s) measured by REBELS: (a) the UV spectral slope, β, such that the specific luminosity $L_\lambda \propto \lambda^\beta$ in the wavelength range $1600 - 2500$Å; (b) the observed UV continuum flux, F_{1500} at 1500Å, (c) the observed far-infrared continuum flux, F_{158}, at $\approx 158\mu m$; we express fluxes in units of μJy. These data are presently available for 14 galaxies[4] in the REBELS sample, whose mean redshift is $\langle z_s \rangle = 7.01$. A summary of the relevant data for the galaxy in the sample is given in Tab. 1. Although our model does not make predictions on the stellar mass, in the Table we also report the M_* values obtained by the REBELS Collaboration (Stefanon+21, in prep.) from rest-frame UV SED fitting[5] using BEAGLE (Chevallard & Charlot 2016). These are only used to check the consistency of the dust SN yield, y_d, reported in the penultimate column of Tab. 2 and Tab. 3.

Before we proceed it is necessary to define L_λ, for which we rely on the stellar population synthesis code STARBURST99 (Leitherer et al. 1999). We assume: (a) continuous star formation, (b) Salpeter Initial Mass Function in the range $1 - 100 M_\odot$, (c) metallicity $Z = 0.004$; all quantities below are computed at a fixed age of 150 Myr. The models adopt Geneva stellar tracks including the early AGB evolution up to the first thermal pulse for masses $> 1.7 M_\odot$. For later use, this IMF produces $\nu_{SN} = (52.89 M_\odot)^{-1}$ supernovae (SN) per unit stellar mass formed.

From the specific luminosity we obtain the conversion factor[6] between the intrinsic (i.e. unattenuated) luminosity, L^*_{1500}, and the star formation rate (SFR) at $\lambda_{1500} = c/\nu_{1500} = 1500$Å :

$$\mathcal{K}_{1500} \equiv \frac{L^*_{1500}}{\text{SFR}} = \frac{(\lambda L^*_\lambda)_{\lambda_{1500}}}{\text{SFR}} = 1.174 \times 10^{10}; \qquad (1)$$

$\mathcal{K}_{1500}$ has units of $L_\odot/(M_\odot \text{yr}^{-1})$. We have tested the dependence of $\mathcal{K}_{1500}$ on the star formation history by considering a $\text{SFR}(t) \propto \exp(t/t_0)$. This form allows to model both increasing (when the timescale $t_0 > 0$) and decreasing ($t_0 < 0$) histories; we have explored the range $1\,\text{Myr} \leq |t_0| < 100\,\text{Myr}$. Increasing histories yield up to 30% higher $\mathcal{K}_{1500}$ values with respect to the constant SFR one; a decreasing SFR lowers $\mathcal{K}_{1500}$ by a factor $\lesssim 2$. As high-z galaxies generally feature a time-increasing SFR (Pallottini et al. 2019, 2022), we consider the value in eq. 1 a reasonable choice.

Similarly, we compute the intrinsic UV spectral slope,

$$\beta_{\text{int}} \equiv \frac{d\ln L_\lambda}{d\ln \lambda} = \frac{\ln(L^*_{\lambda_1}/L^*_{\lambda_2})}{\ln(\lambda_1/\lambda_2)} = -2.406, \qquad (2)$$

where $(\lambda_1, \lambda_2) = (1600, 2500)$Å. From the input data we build a non-dimensional *molecular index*,

$$I_{\text{m}} = \frac{(F_{158}/F_{1500})}{(\beta - \beta_{\text{int}})}, \qquad (3)$$

whose physical meaning will be discussed later on. The derived values of I_{m} are given in Tab. 1 for each galaxy in the sample.

2.1. *From UV slope to optical depth*

Converting β into a dust optical depth, τ_λ, involves the knowledge of the dust extinction curve, and a model for the radiative transfer (RT) of stellar radiation through dust. We adopt two extinction curves, both taken from Weingartner & Draine (2001, WD01), appropriate for the (a) Milky Way with extinction factor $R_V = 3.1$ (hereafter MW), and (b) SMC bar (SMC).

The extinction cross-sections are normalized to the SB99 metallicity $Z = 0.004$ by assuming a linear scaling with metallicity for which we set $Z_{MW} = 0.0142$ (i.e., the solar value, Asplund et al. 2009) and $Z_{SMC} = 1.63 \times$

---

[4] These are the only galaxies with dust continuum detection out of the 40 targets of the full REBELS sample. Among the 14 galaxies listed in Tab. 1, 13 have also a [CII] line measurement. REBELS-06 is undetected in [CII] and therefore only the photo-z is available for this source. However, observations of the source are still ongoing and [CII] may still be found.

[5] The authors adopt a constant star formation history, $Z = 0.2Z_\odot$, a Calzetti et al. (2000) dust extinction law, and a Chabrier (2003) $0.1 - 300 M_\odot$ IMF. Note that the correction on M_*, in principle required for consistency with the metallicity value and Salpeter IMF used here, is well within uncertainties reported in Tab. 1, and thus it does not significantly affect our results. We warn that using non-parametric prescriptions for the star formation history might result in M_* values on average up to $\approx 3\times$ higher (Topping et al., in prep).

[6] The choice of the Salpeter IMF is motivated by consistency with the standard conversion from specific UV luminosity to SFR $\text{SFR}[M_\odot \text{yr}^{-1}] = 1.4 \times 10^{-28} L_\nu(1500\text{Å}) \,[\text{erg s}^{-1}\text{Hz}^{-1}]$ typically used by high-z surveys (e.g. Oesch et al. 2014) which is based on such IMF (Kennicutt 1998; Madau & Dickinson 2014). Written in this form, the numerical factor corresponding to our $\mathcal{K}_{1500}$ is equivalent to 4.45×10^{-29}; the $\approx 3\times$ difference arises from the subsolar ($Z = 0.004$) metallicity assumed here.

Table 1. Measured REBELS galaxy properties and adopted relative errors. For F_{1500} we have assumed a 20% error (corresponding to ≈ 0.2 mag on $M_{\rm UV}$). Galaxy names in the text are abbreviated as REBxx for conciseness.

			REBELS DATA			
# ID	z	β	F_{1500}	F_{158}	I_m	$\log(M_*/M_\odot)$
			μJy	μJy		
REBELS-05	6.496	$-1.29^{+0.36}_{-0.44}$	0.315±0.063	67.2±12.7	191.1^{+75}_{-84}	$9.16^{+0.85}_{-1.00}$
REBELS-06	6.800	$-1.24^{+0.67}_{-0.35}$	0.329±0.066	76.7±15.3	200.2^{+122}_{-80}	$9.50^{+0.45}_{-0.79}$
REBELS-08	6.749	$-2.17^{+0.58}_{-0.58}$	0.363±0.073	101.4±19.8	1183.0^{+457}_{-457}	$9.02^{+0.64}_{-0.68}$
REBELS-12	7.349	$-1.99^{+0.48}_{-0.76}$	0.543±0.109	86.8±24.3	384.3^{+161}_{-197}	$8.94^{+0.93}_{-0.70}$
REBELS-14	7.084	$-2.21^{+0.41}_{-0.47}$	0.704±0.141	60.0±14.7	434.9^{+159}_{-166}	$8.73^{+0.80}_{-0.70}$
REBELS-18	7.675	$-1.34^{+0.19}_{-0.32}$	0.448±0.090	52.9±9.9	110.7^{+34}_{-40}	$9.49^{+0.56}_{-0.73}$
REBELS-19	7.369	$-2.33^{+0.45}_{-0.64}$	0.242±0.048	71.2±20.4	3869.6^{+1544}_{-1719}	$8.79^{+0.69}_{-0.69}$
REBELS-25	7.306	$-1.85^{+0.56}_{-0.46}$	0.263±0.053	259.5±22.2	1772.0^{+660}_{-585}	$9.89^{+0.15}_{-0.18}$
REBELS-27	7.090	$-1.79^{+0.42}_{-0.45}$	0.359±0.072	50.6±9.9	229.0^{+84}_{-86}	$9.69^{+0.25}_{-0.34}$
REBELS-29	6.685	$-1.61^{+0.10}_{-0.19}$	0.547±0.109	56.1±12.9	128.8^{+40}_{-42}	$9.62^{+0.19}_{-0.19}$
REBELS-32	6.729	$-1.50^{+0.28}_{-0.30}$	0.313±0.062	60.4±17.1	213.2^{+84}_{-85}	$9.55^{+0.35}_{-0.37}$
REBELS-38	6.577	$-2.18^{+0.45}_{-0.42}$	0.404±0.081	163.0±22.8	1786.5^{+571}_{-555}	$9.58^{+0.74}_{-1.27}$
REBELS-39	6.847	$-1.96^{+0.30}_{-0.28}$	0.798±0.160	79.7±16.2	224.1^{+72}_{-71}	$8.56^{+0.57}_{-0.57}$
REBELS-40	7.365	$-1.44^{+0.29}_{-0.36}$	0.302±0.060	48.3±12.9	165.3^{+64}_{-69}	$9.48^{+0.45}_{-0.99}$

10^{-3} (Choudhury et al. 2018) for the MW and SMC, respectively.

By generalizing eq. 2 to the observed (attenuated) luminosity, $L_\lambda = L^*_\lambda T_\lambda$, where $T_\lambda(\tau_\lambda)$ is the UV dust transmissivity (see below) one can write

$$\beta = \beta_{\rm int} - 2.24 \ln\left(\frac{T_{\lambda_1}}{T_{\lambda_2}}\right);$$ (4)

note that for a flat transmissivity ($T_\lambda \approx$ const.), $\beta = \beta_{\rm int}$, independently of optical depth.

We pause to emphasise that there is a distinction between the *physical* value, τ_λ, of the optical depth (entering eqs. 5 and 8 below), and the *effective* one deduced from the flux attenuation, $\tau_{\rm eff} = -\ln T$. While $\tau_{\rm eff}$ depends on the radiative transfer properties, τ_λ is determined, as we will see below, by the galaxy dust mass and distribution only.

The functional form of T_λ depends on radiative transfer, and therefore on the optical properties of dust grains (the wavelength-dependent albedo, ω, and asymmetry parameter, g, i.e. the mean cosine of the scattering angle), and relative spatial distribution of stars and dust[7]. To bracket such uncertainty we consider two possibilities (although we have experimented with additional ones): (a) a slab geometry in which stars and dust are mixed

but have different scale heights; (b) a spherical dust distribution with a central source including scattering.

These two geometries should mimic the two typical evolutionary stages, both predicted (Pallottini et al. 2019; Kohandel et al. 2019, 2020) and observed (Jones et al. 2017; Smit et al. 2018) in high-z galaxies, resulting from a periodic switch from a well-designed proto-disk (slab geometry), and a more isotropic (spherical) configuration induced by frequent merging events.

□ *Slab geometry.* Baes & Dejonghe (2001) found the solution for a slab of total optical depth τ_λ, in which dust and stars both follow a vertical exponential distribution with a ratio of scale heights $\zeta = h_d/h_*$. The transmissivity is

$$T_\lambda = \frac{1}{\mu} e^{-\frac{(1-\omega)}{2\mu}\tau_\lambda} \mathcal{W}_\zeta\left[\frac{(1-\omega)\tau_\lambda}{2\mu}\right].$$ (5)

In the previous equation, $\mu = \cos\theta$, denotes the direction making an angle $\arccos\mu$ with the face-on direction $\mu = 1$. We fix this value to the most probable inclination for randomly oriented galaxies, $\mu = \cos(\pi/2 - 1) =$

---

[7] The values of ω and g are consistently computed from the adopted WD01 MW and SMC curves. For reference, at 1500Å: $\omega = (0.3807, 0.4170)$, $g = (0.6633, 0.5756)$ for (MW, SMC).

0.841. Finally[8],

$$W_\zeta(x) = \zeta \int_0^1 (1-t)^{\zeta-1} \cosh(xt)dt. \qquad (7)$$

□ *Spherical geometry.* The classical Code (1973) solution for a spherical dust distribution, obtained with the two-stream approximation and confirmed by Monte Carlo radiative transfer simulations (Ferrara et al. 1999; Krügel 2009; Di Mascia et al. 2021a), is

$$T_\lambda = \frac{2}{(1+\eta)e^{\xi\tau_\lambda} + (1-\eta)e^{-\xi\tau_\lambda}}, \qquad (8)$$

where

$$\eta = \sqrt{(1-\omega)/(1-\omega g)}; \quad \xi = \sqrt{(1-\omega)(1-\omega g)}. \quad (9)$$

Eq. 8 reduces to the standard $e^{-\tau_\lambda}$ screen solution for pure absorption ($\omega = 0$).

Armed with the expressions for T_λ for the slab and spherical cases, and with the help of eq. 4, we can derive the optical depth at 1500Å, τ_{1500}, of a galaxy with spectral slope β (Fig. 1). For a given β value, slab configurations (we show the case $\zeta = 2$ as an example) are more transparent than spherical ones, i.e. they require a larger optical depth to produce the same slope. Also, SMC curves are more opaque than MW ones, i.e. they require less dust to produce the same β value.

Due to their larger transparency, slab geometries cannot produce arbitrarily large β values for the MW curve, as indicated by the vertical asymptote at $\beta_{max} \approx -0.9$. The value of β_{max} increases with ζ, i.e. as the solution progressively approximates a more opaque screen geometry. Reproducing the measured β values in REBELS (grey lines in Fig. 1) imposes a lower limit $\zeta \gtrsim 1.7$ when using the MW curves. For this reason, and because increasing ζ to values > 2 has no effect on our results, we set $\zeta = 2$ from now on. As an illustration, for a MW dust slab the galaxies in the sample have $0.92 < \tau_{1500} < 8.44$, but $1.01 < \tau_{eff} < 2.35$, i.e. they are effectively only mildly optically thin[9].

2.2. *From optical depth to dust mass*

To derive the dust mass, M_d, we start by writing the following relation:

$$\tau_{1500} = \frac{1}{\pi m_p f_\mu} \frac{M_d}{r_d^2} \sigma_{1500}, \qquad (10)$$

---

[8] Note that if stars and dust are homogeneously mixed ($\zeta = 1$), and scattering is neglected ($\omega = 0$), $W_\zeta = x^{-1}\sinh x$ and eq. 5 reduces to the more familiar formula

$$T_\lambda = \frac{(1 - e^{-\tau_\lambda/\mu})}{\tau_\lambda}. \qquad (6)$$

[9] The 1500Å to V-band conversion is $\tau_{1500} = (2.655, 5.319)\tau_V$ for (MW, SMC) curves, respectively.
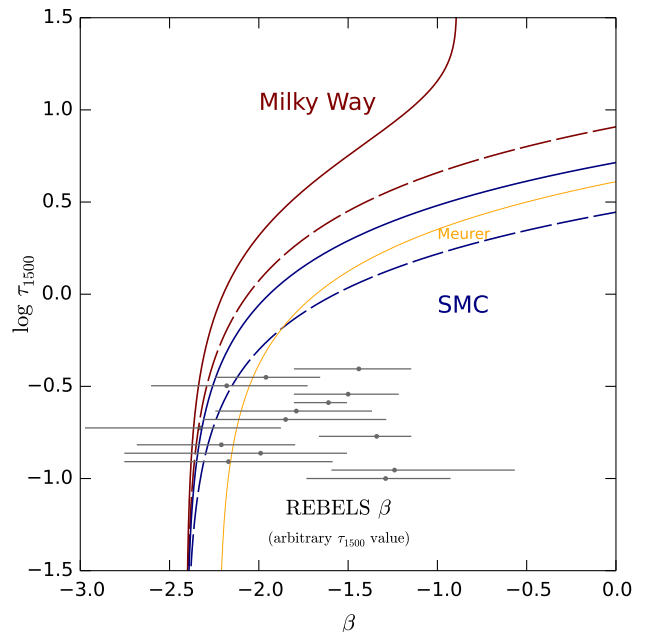
Figure 1. Relation between optical depth at 1500Å, τ_{1500}, and UV spectral slope, β, often referred to as the *attenuation* curve, for the Milky Way (red curves) and SMC (blue) for a slab (solid) and spherical (dashed) geometry with $\zeta = 2$ (i.e., the dust scale height is twice the stellar one). Also shown for reference is the empirical Meurer et al. (1999) relation (orange) $\tau_{1600} = 4.43 + 1.99\beta$. The β values for the 14 REBELS sources with 158μm continuum detections are shown by grey points/lines at arbitrary τ_{1500} values.

where m_p is the proton mass[10], r_d is the (unknown) radius of the spherical or disk-like (for the slab approximation) dust distribution, and $\sigma_{1500} = (3.66, 7.25) \times 10^{-22}\text{cm}^2$ is the WD01 (MW, SMC) dust extinction cross section at 1500Å, scaled to the appropriate metallicity (see Sec. 2.1). The factor f_μ is a geometrical correction; it is $f_\mu = (4/3, \mu)$ for a homogeneous sphere or a disk[11], respectively. Inserting the numerical factors, eq. 10 is rewritten as

$$M_d = f_\mu \frac{\tau_{1500}}{\tau_0} \left(\frac{r_d}{\text{kpc}}\right)^2 M_\odot, \qquad (11)$$

where $\tau_0 = (1.09, 2.17) \times 10^{-8}$ for (MW, SMC).

2.3. *Star formation rate and infrared luminosity*

---

[10] For simplicity, we have assumed a pure hydrogen gas with unity mean molecular weight.

[11] For a disk, this f_μ expression is valid as long as the viewing angle $\theta < \pi/2 - \arctan(h_d/r_d)$, which for our choice of μ is always satisfied if $h_d/r_d < 1$.

Having determined τ_{1500} and the corresponding value of T_{1500} from eqs. 5 and 8, for each REBELS galaxy we can straightforwardly derive two important quantities: the total SFR, and the total FIR luminosity, $L_{\rm IR}$, typically computed in the range $8-1000\,\mu m$. Recalling eq. 1, the SFR is obtained from the observed UV flux:

$$F_{1500} = \frac{g(z_s)}{4\pi\nu_{1500}}\mathcal{K}_{1500}\,T_{1500}\,\mathrm{SFR}; \qquad (12)$$

$g(z_s) = (1+z_s)/d_L^2$, where d_L is the luminosity distance to the galaxy located at redshift z_s. The observed total FIR luminosity is then

$$L_{\rm IR} = \alpha\frac{(1-T_{1500})}{T_{1500}}L_{1500} = \mathrm{IRX}\,L_{1500}, \qquad (13)$$

which shows that the so-called infrared excess parameter $\mathrm{IRX} \equiv L_{\rm IR}/L_{1500} = \alpha(1-T_{1500})/T_{1500}$. The $\mathcal{O}(1)$ coefficient α represents the UV bolometric absorption correction (dust is heated also by UV photons with $\lambda \neq \lambda_{1500}$); for simplicity we set $\alpha = 1$ in the following.

Finally, a quantity that is often reported in the literature is the *observed* star formation fraction, $f_{\rm obs}$. Using the previous results, it is easy to show that $f_{\rm obs}$ can be related to IRX or T_{1500}:

$$f_{\rm obs} = \frac{L_{1500}}{L_{1500} + L_{\rm IR}} = \frac{1}{1 + \mathrm{IRX}} = T_{1500}. \qquad (14)$$

2.4. Dust temperature

Dust grains are heated by absorption of UV photons and re-emit such energy in the FIR. The emitted radiation spectrum is usually modelled as a grey-body from which the mean dust temperature, $\bar{T}_d$, can be derived:

$$\bar{T}_d = \left(\frac{L_{\rm IR}}{\Theta M_d}\right)^{1/(4+\beta_d)}; \qquad (15)$$

where

$$\Theta = \frac{8\pi}{c^2}\frac{\kappa_{158}}{\nu_{158}^{\beta_d}}\frac{k_B^{4+\beta_d}}{h_P^{3+\beta_d}}\zeta(4+\beta_d)\Gamma(4+\beta_d). \qquad (16)$$

The mass absorption coefficient, $\kappa_\nu = \kappa_{158}(\nu/\nu_{158})^{\beta_d}$ is pivoted at wavelength $\lambda_{158} = c/\nu_{158} = 158\mu m$ since high-z ALMA observations are often tuned to the rest wavelength of [CII] emission. We take κ_{158} and β_d consistently with the adopted WD01 extinction curve $\kappa_{158} = (10.41, 13.55)\,\mathrm{cm}^2\mathrm{g}^{-1}$, and $\beta_d = (2.03, 2.07)$ for (MW, SMC); ζ and Γ are the Zeta and Gamma functions, respectively. Other symbols have the usual meaning. We then find $\Theta = (4.89, 5.33) \times 10^{-6}$ for (MW, SMC).

We define the temperature in eq. 15 as the mean *physical* dust temperature. Such value corresponds to the temperature dust grains would attain should the available UV energy being uniformly distributed among them. This is possible only if the system is optically thin, i.e. $\tau_{1500} \ll 1$. In general, though, radiative transfer effects produce a temperature distribution, with T_d decreasing away from the source. Although radiative transfer is a complex problem which can be fully treated with detailed numerical simulations[12] (see, e.g. Behrens et al. 2018; Liang et al. 2019), we nevertheless try to approximately take into account this effect for the simple geometry adopted here.

In App. A we show that the luminosity-weighted temperature,$\langle T_d\rangle_L$, of an absorbing dust layer depends on its total optical depth, and can be written as

$$\langle T_d\rangle_L = \bar{T}_d\,\frac{6}{7}\tau_{1500}^{1/6}\frac{(1-e^{-7\tau_{1500}/6})}{(1-e^{\tau_{1500}})^{7/6}} \equiv \bar{T}_d f_L(\tau_{1500}). \quad (17)$$

For the τ_{1500} values deduced for REBELS galaxies, applying eq. 17 results in temperatures that are $\lesssim 20\%$ higher than $\bar{T}_d$ (see Fig. 7). As discussed in App. A, to conserve energy M_d in eq. 11 must be reduced by a factor $f_L^{-(4+\beta_d)}$, which might result in a $(2-3)\times$ lower mass estimate. In the following we denote this reduced dust mass by $M_d' = f_L^{-(4+\beta_d)}M_d$.

2.5. Observed flux at 158μm

From the previous results it is straightforward to compute the rest frame $158\mu m$ specific flux observed at $\lambda = 158(1+z_s)\,\mu m$:

$$F_{158} = g(z_s)\,\kappa_{158}M_d'[B_{158}(T_d') - B_{158}(T_{\rm CMB})]; \quad (18)$$

B_λ is the black-body spectrum, and $T_{\rm CMB}(z) = T_0(1+z)$, with $T_0 = 2.7255$ K (Fixsen 2009) is the CMB temperature at redshift z. Equation 18 accounts for the fact that the CMB acts as a thermal bath for dust grains, setting a lower limit to their temperature. At $z = 7$ such minimum temperature corresponds to $T_{\rm CMB} = 21.8$ K. Finally, T_d' is the CMB-corrected dust temperature[13] following Da Cunha et al. (2013),

$$T_d' = \{\langle T_d\rangle_L^{4+\beta_d} + T_0^{4+\beta_d}[(1+z)^{4+\beta_d} - 1]\}^{1/(4+\beta_d)}. \quad (19)$$

Note that both M_d' and T_d' depend on the radial extent of the dust distribution, r_d (see eq. 11 and 15). The latter can be obtained by imposing that F_{158} from eq. 18 matches the corresponding observed flux for each galaxy in the REBELS sample.

---

[12] These two works use the SKIRT code (skirt.ugent.be) to post-process the simulation outputs.

[13] In the remainder of the paper we will always refer to dust temperature as the *CMB-corrected* one, i.e. T_d' in eq. 19.

3. RESULTS

Before discussing the results, let us briefly summarize our method, also illustrated schematically in Fig. 2. We use three observables measured by REBELS for 14 galaxies: these are β, F_{1500}, and F_{158}. From β, for given a RT model (i.e. transmissivity T_{1500}, also equal to $f_{\rm obs}$) and extinction curve, we determine τ_{1500}, and hence the dust mass M'_d, modulo the dust distribution radius, r_d. We then use F_{1500} to determine the total SFR and $L_{\rm IR} = {\rm IRX}\, L_{1500}$, which then form the basis to compute the (RT+CMB)-corrected, luminosity-weighted dust temperature T'_d, and F_{158}. Finally, by imposing that F_{158} matches the observed 158μm flux, we determine r_d (the only free parameter[14] of the model once the extinction curve and the RT geometry have been fixed) for each galaxy.

Hence, from 3 data inputs (β, F_{1500}, F_{158}), our model can predict 7 physical properties for each galaxy (τ_{1500}, T_{1500}, SFR, $L_{\rm IR}$, T'_d, M'_d, r_d). By construction, a galaxy with the set of derived properties matches the observed 1500Å and 158μm continuum data.

Finally, we note that, in some cases, a solution cannot be found because the observed 158μm flux cannot be retrieved from the input F_{1500} and β values. To see this let us inspect Fig. 3. As an example, there we consider the MW extinction, slab geometry case. The Figure illustrates the final step of the method sketched in Fig. 2, i.e. the determination of r_d. This is derived by matching the predicted F_{158} to the observed one for each galaxy. The F_{158} trend with r_d can be understood as follow. As $M'_d \propto r_d^2$, F_{158} initially increases due the larger amount of emitting material. However, T'_d (golden squares) decreases as the dust distribution becomes more extended until it approaches $T_{\rm CMB}$. At that point F_{158} reaches a plateau independent of r_d. The plateau level increases with τ_{1500}: from Fig. 3 and Tab. 2 we see that REBELS-06 – the most opaque ($\tau_{1500} = 8.44$) system – has the potentially highest 158μm flux, ≈ 3 mJy.

Thus, for a given τ_{1500}, the 158μm flux cannot be arbitrarily large. If the observed F_{158} for a galaxy exceeds this value, the method does not yield a solution. In the MW case, for example, this occurs for 4 (REBELS-08,19,25,38) out of 14 galaxies in the sample (see Tab. 2). We discuss the interpretation of these no-solution cases in Sec. 5. For the well-behaved galaxies we find sub-kpc r_d values implying that at the REBELS spatial resolution (≈ 1.2 arcsec or 6.3 kpc at $z = 7$) these objects are unresolved.

---

[14] Note that the spatial resolution of the REBELS survey (≈ 7 kpc) is much larger than the $r_d \lesssim 1$ kpc values obtained here.
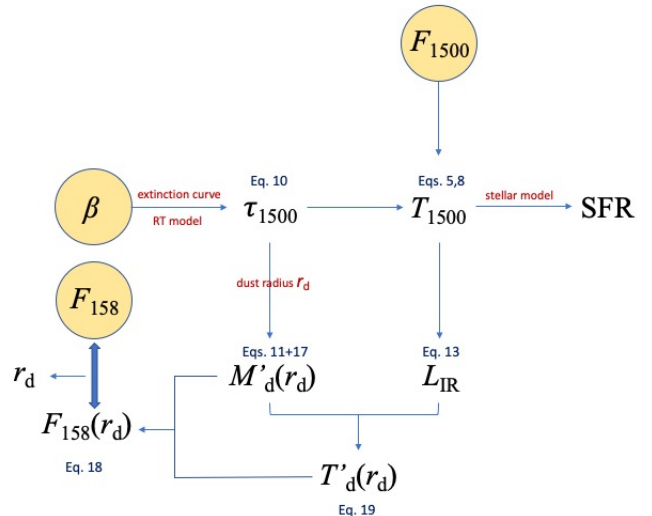

Figure 2. Schematic overview of the method. Yellow circles denote the three input observables measured by REBELS; red text indicates assumptions made in that step. Equations defining the different quantities in the text are indicated (blue).

We next discuss our results separately for MW and SMC extinction curves, and highlight the differences induced by the adopted RT (slab/spherical) model for each curve.

3.1. Milky Way extinction curve

The full results for this case are reported in Tab. 2, and displayed graphically in Fig. 4. First of all we note that our method provides a self-consistent solution matching the data for 10 out of 14 galaxies in the sample. These solutions are presented in the following. The interpretation and implications of no-solution cases will be instead discussed in Sec. 5.

3.1.1. Slab geometry

Starting from the slab geometry case, the results indicate that $\tau_{1500} = 2.655\tau_V$ varies from 0.92 to 8.44, i.e. galaxy are physically optically thick at 1500Å but mildly so in the V-band and in terms of the effective optical depth, $\tau_{\rm eff}$ (see discussion in Sec. 2.1). This range translates in transmissivity values going from 9.5% to 72%, the most star-forming galaxies being the most obscured. Since $T_{1500} = f_{\rm obs}$ (see eq. 14), we conclude that $28 - 90.5\%$ of the star formation at high-z is obscured, if the REBELS targets fairly sample early galaxy populations.

The deduced total star formation rates are relatively sustained, $31.5 < {\rm SFR}/({\rm M}_\odot{\rm yr}^{-1}) < 129.5$ with REBELS-14 (REBELS-18) being the least (most) star
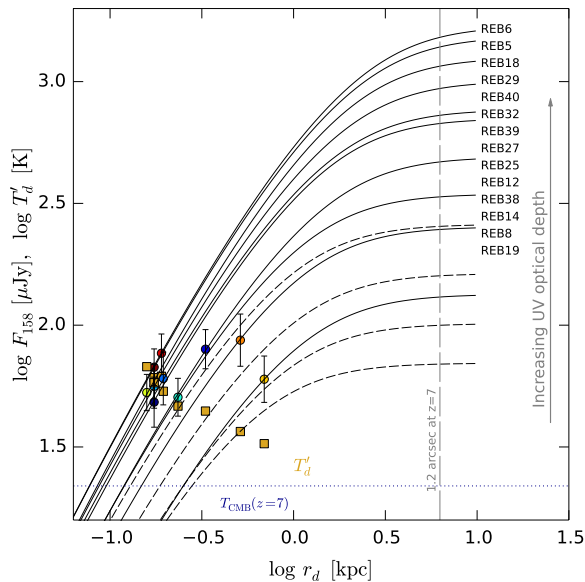
Figure 3. Predicted F_{158} flux (curves; ordered as the galaxy name list) as a function of dust radius, r_d, for each galaxy in the REBELS sample. Curves are shown for MW extinction, slab geometry case reported in Tab. 2. The measured value of F_{158} (points) is used to determine r_d for each system (see Fig. 2). For 4 galaxies (REBELS-08,19,25,38) no solution can be found as their F_{158} flux is too high to be matched by the corresponding curve (dashed lines). Also shown is the luminosity-weighted dust temperature, T'_d (squares), and the angular resolution (vertical line) of the survey.

forming system, with a mean SFR = 65.8 $M_\odot \mathrm{yr}^{-1}$. The ratio between the total IR luminosity and the SFR, which we define as $\mathcal{K}_{\mathrm{IR}}$ paralleling eq. 1, varies from $\mathcal{K}_{\mathrm{IR}} \simeq 10^{10} L_\odot/(M_\odot \mathrm{yr}^{-1})$ for the most star-forming galaxy to $\mathcal{K}_{\mathrm{IR}} \simeq 3.3 \times 10^9 L_\odot/(M_\odot \mathrm{yr}^{-1})$ towards the lower end of the SFR range, corresponding to a factor ≈ 3 decrease. Thus, the specific IR luminosity of low-SFR galaxies is lower than expected for vigorously star-forming ones. We note in passing that the value $\mathcal{K}_{\mathrm{IR}} \simeq 10^{10} L_\odot/(M_\odot \mathrm{yr}^{-1})$ matches the commonly assumed one prescribed by Kennicutt (1998).

Our model also constrains dust properties. The 10 systems for which a solution can be found all contain considerable amounts of dust at luke-warm temperatures. The sample-averaged dust mass and temperature are $(1.3 \pm 1.1) \times 10^7 M_\odot$ and 52 ± 11 K, respectively. However, in some galaxies dust is particularly abundant (REBELS-14, $M'_d \approx 3.4 \times 10^7 M_\odot$), or hot (REBELS-18, $T'_d \approx 67$ K). The dust distribution is compact as one can infer from the values of r_d. These are all sub-kpc, with 70% of the galaxies showing $r_d < 0.3$ kpc. Such compact configuration, in general, produces high

dust temperatures: the hottest REBELS-18 indeed is the most compact one with only $5 \times 10^6 M_\odot$ of dust concentrated in a very small region ($r_d = 0.16$ kpc). As a caveat, we note that the implied compactness might partly be due to the adopted geometry, such that actual observed sizes could be larger if the dust/starlight are more inhomogenously distributed.

Finally, by using the stellar mass, M_*, obtained by the REBELS Collaboration from SED fitting, we estimate the dust yield per supernova[15], $y_d = M'_d/\nu_{\mathrm{SN}} M_*$. Although *this is not a self-consistent output*, as it uses an independent estimate of M_*, it nevertheless represents a useful reference. We find $0.1 \leq y_d/M_\odot \leq 3.3$ with a mean value $\langle y_d \rangle = 0.9 M_\odot$ with 7 (out of 10) galaxies requiring $y_d < 0.25 M_\odot$. As already mentioned in Sec. 2, stellar masses determined assuming a nonparametric star formation history might be on average a factor ≈ 3 larger. In this case the SN yield would be correspondingly decreased to $0.03 \leq y_d/M_\odot \leq 1.1$. Such dust yield range is in good agreement with available estimates (Todini & Ferrara 2001; Hirashita et al. 2015; Marassi et al. 2015, 2019; Gall & Hjorth 2018; Leśniewska & Michałowski 2019) which typically indicate $y_d = 0.01 - 0.45 M_\odot$ (for a review see Cherchneff 2014). Note, however, that even higher values are found, as in the case of the Cas A remnant for which $y_d = 0.99^{+0.10}_{-0.09} M_\odot$ (Priestley et al. 2019; Niculescu-Duvaz et al. 2021), or G54.1+0.3 for which $0.3 < y_d < 0.9$ (Temim et al. 2017; Rho et al. 2018). However, three galaxies (REBELS-12, 14, 39) require $y_d > 1 M_\odot$, which is likely inconsistent with pure SN production, and might require dust growth via accretion of heavy elements from the ISM (e.g. Mancini et al. 2015; Popping et al. 2017; Graziani et al. 2020).

3.1.2. *Spherical geometry*

Let us now consider the spherical case. The key difference between the two cases is due to the fact that, for a given extinction curve, spherical geometries are more opaque (see Fig. 1). This implies that a given β value can be reproduced with a smaller τ_{1500}, and yields a slightly lower T_{1500} (see Tab. 2). The resulting star formation rates are essentially unaltered, and now span the range $31.9 < \mathrm{SFR}/(M_\odot \mathrm{yr}^{-1}) < 145.4$; REBELS-14 (REBELS-18) are confirmed to be the least (most) star forming system. Quantities related to dust differ only by a few percent; specifically, we find on average fractional

---

[15] We neglect dust production from AGB stars ($2 < M/M_\odot < 8$ as their evolutionary time is longer than the Hubble time at $z \approx 7$. Critical issues related to dust growth at early times are discussed in Ferrara et al. (2016); Ferrara & Peroux (2021).

Table 2. Best-fit measured and derived REBELS galaxy properties for a MW extinction curve and different geometries.

	SLAB GEOMETRY												
β	F_{1500}	F_{158}	M_*	ID#	τ_{1500}	T_{1500}	SFR	$L_{\rm IR}$	T'_d	M'_d	r_d	y_d	κ_s
	Measured						*Derived*						
	μJy	μJy	$M_\odot$				$M_\odot\,\mathrm{yr}^{-1}$	$L_\odot$	K	$M_\odot$	kpc	$M_\odot$	
-1.29	0.315	67.2	1.45e+09	REBELS-05	7.755	0.109	81.9	8.57e+11	60.9	5.91e+06	0.174	0.22	10.1
-1.24	0.329	76.7	3.16e+09	REBELS-06	8.438	0.095	105.2	1.12e+12	61.8	7.05e+06	0.190	0.12	10.8
-2.17	0.363	101.4	1.05e+09	REBELS-08	...	...	...	...	...	...	...	...	...
-1.99	0.543	86.8	8.71e+08	REBELS-12	2.085	0.488	37.7	2.27e+11	36.7	3.47e+07	0.508	2.11	0.9
-2.21	0.704	60.0	5.37e+08	REBELS-14	0.924	0.719	31.5	1.04e+11	32.6	3.38e+07	0.693	3.33	1.0
-1.34	0.448	52.9	3.09e+09	REBELS-18	7.143	0.125	129.5	1.33e+12	67.3	5.01e+06	0.160	0.09	18.8
-2.33	0.242	71.2	6.17e+08	REBELS-19	...	...	...	...	...	...	...	...	...
-1.85	0.263	259.5	7.76e+09	REBELS-25	...	...	...	...	...	...	...	...	...
-1.79	0.359	50.6	4.90e+09	REBELS-27	3.301	0.335	34.4	2.69e+11	46.5	9.45e+06	0.235	0.10	2.8
-1.61	0.547	56.1	4.17e+09	REBELS-29	4.591	0.233	69.4	6.25e+11	58.1	5.68e+06	0.174	0.07	9.0
-1.50	0.313	60.4	3.55e+09	REBELS-32	5.514	0.183	50.9	4.88e+11	53.4	7.42e+06	0.197	0.11	5.0
-2.18	0.404	163.0	3.80e+09	REBELS-38	...	...	...	...	...	...	...	...	...
-1.96	0.797	79.7	3.63e+08	REBELS-39	2.256	0.462	52.9	3.34e+11	44.2	1.59e+07	0.335	2.31	2.8
-1.44	0.302	48.3	3.02e+09	REBELS-40	6.077	0.160	64.4	6.35e+11	58.2	5.73e+06	0.172	0.10	8.2

	SPHERICAL GEOMETRY												
β	F_{1500}	F_{158}	M_*	ID#	τ_{1500}	T_{1500}	SFR	$L_{\rm IR}$	T'_d	M'_d	r_d	y_d	κ_s
	Measured						*Derived*						
	μJy	μJy	$M_\odot$				$M_\odot\,\mathrm{yr}^{-1}$	$L_\odot$	K	$M_\odot$	kpc	$M_\odot$	
-1.29	0.315	67.2	1.45e+09	REBELS-05	3.467	0.099	90.4	9.56e+11	62.5	5.61e+06	0.165	0.21	11.4
-1.24	0.329	76.7	3.16e+09	REBELS-06	3.637	0.088	113.0	1.21e+12	62.9	6.80e+06	0.180	0.11	11.7
-2.17	0.363	101.4	1.05e+09	REBELS-08	...	...	...	...	...	...	...	...	...
-1.99	0.543	86.8	8.71e+08	REBELS-12	1.186	0.463	39.7	2.51e+11	37.9	3.12e+07	0.547	1.89	1.2
-2.21	0.704	60.0	5.37e+08	REBELS-14	0.539	0.709	31.9	1.09e+11	33.2	4.72E+07	0.788	3.12	1.2
-1.34	0.448	52.9	3.09e+09	REBELS-18	3.298	0.111	145.4	1.52e+12	69.4	4.72e+06	0.152	0.08	22.0
-2.33	0.242	71.2	6.17e+08	REBELS-19	...	...	...	...	...	...	...	...	...
-1.85	0.263	259.5	7.76e+09	REBELS-25	...	...	...	...	...	...	...	...	...
-1.79	0.359	50.6	4.90e+09	REBELS-27	1.810	0.304	37.9	3.10e+11	48.3	8.58e+06	0.243	0.09	3.6
-1.61	0.547	56.1	4.17e+09	REBELS-29	2.395	0.205	78.9	7.36e+11	60.5	5.23e+06	0.173	0.07	11.5
-1.50	0.313	60.4	3.55e+09	REBELS-32	2.760	0.160	58.3	5.75e+11	55.7	6.78e+06	0.190	0.10	6.3
-2.18	0.404	163.0	3.80e+09	REBELS-38	...	...	...	...	...	...	...	...	...
-1.96	0.797	79.7	3.63e+08	REBELS-39	1.278	0.435	56.1	3.72e+11	45.6	1.47e+07	0.364	2.14	3.5
-1.44	0.302	48.3	3.02e+09	REBELS-40	2.961	0.140	73.6	7.43e+11	60.5	5.28e+06	0.165	0.09	10.1

Note—F_{158} fluxes are uncorrected for CMB effects. $L_{\rm IR}$ is computed from UV properties using eq. 13; it therefore might differ from the value obtained by Inami et al. 2021, in prep. which uses a different method.

differences of $(12, 3, 8)\%$ for $(L_{\rm IR}, T'_d, M'_d)$, respectively. Similar small differences are found also for r_d and y_d. We can conclude that for a MW extinction curve, our results are not particularly sensitive to RT effects related to dust geometry. We confirm that no solutions can be found for the same 4 galaxies as in the slab case.

Adopting a SMC curve produces noticeable changes in the estimated galaxy properties reported in Tab. 3. As it is clear from Fig. 1, the MW curve is more transparent than SMC, i.e. it requires a larger τ_{1500} to produce the same β value. This feature is reflected in both the slab and spherical solutions which we discuss next; it also limits to 7 (3) the number of galaxies for which a self-

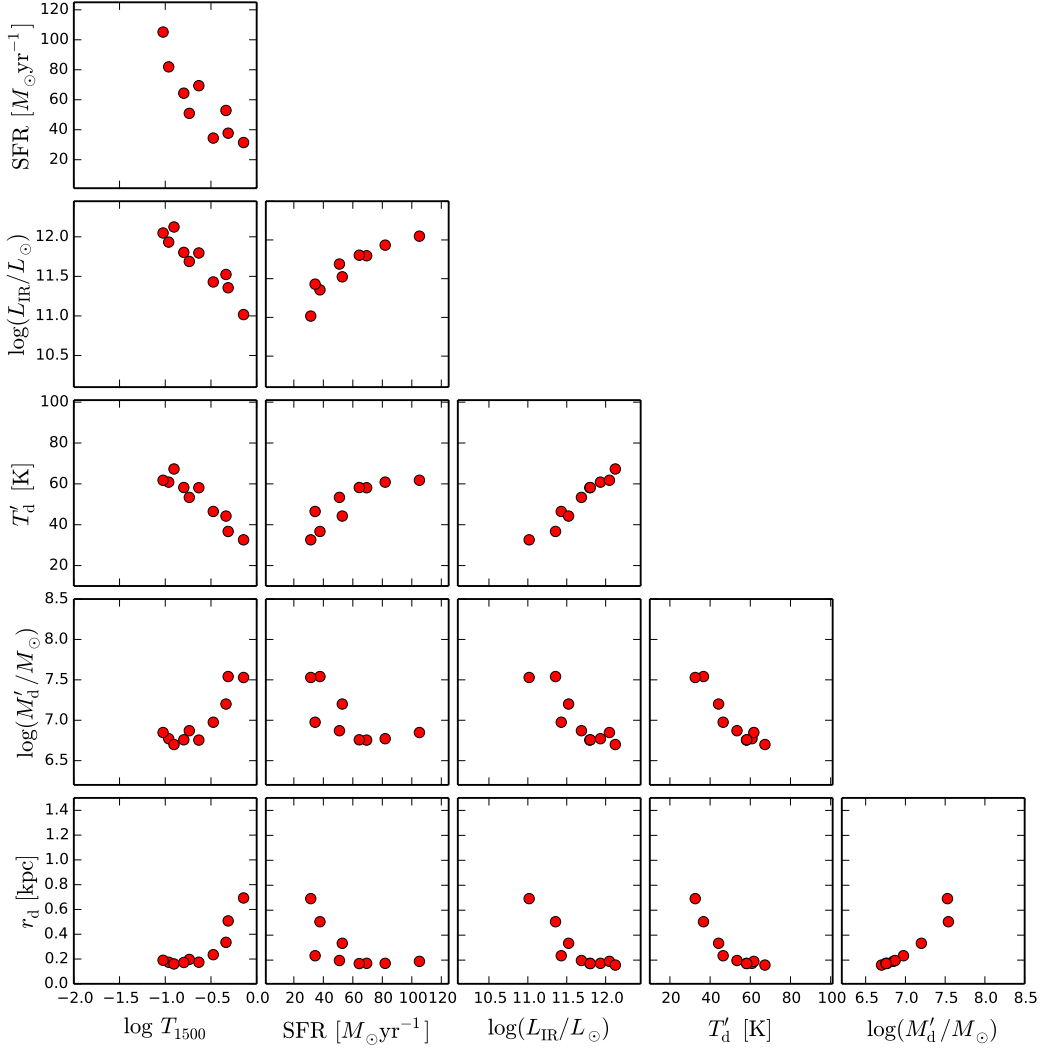### 3.2. *SMC extinction curve*

Figure 4. Overview of the model results for the MW extinction curve and slab geometry case. The shown properties are those reported in Tab. 2 for the 10 REBELS galaxies (red points) for which a solution can be found.

consistent solution can be found in the slab (spherical) geometry cases explored.

3.2.1. *Slab geometry*

With respect to the MW, SMC extinction curves result in a lower UV optical depth ($\tau_{1500} < 2.7$) and larger transmissivity, or observed star formation fraction (eq. 14), $T_{1500} > 0.42$. In turn, these properties determine SFR values that are on average ≈ 3 times lower, with the largest discrepancy (factor ≈ 4) found for the most absorbed galaxies (such as REBELS-06, $\tau_{1500} = 2.71$), or equivalently reddest UV slope.

The total IR luminosity/SFR ratio, is on average lower than for MW curves ($9.6 \lesssim \log \mathcal{K}_{IR} \lesssim 9.8$); it similarly shows an increasing trend with SFR, however without reaching the plateau observed for the MW case at high SFR. Although surprising to a first sight, as SFRs are lower, this result is determined by the even more pronounced decrease of L_{IR} (compare the MW and SMC cases in Tab. 2 and 3) when SMC curves are adopted. As the galaxies are now less star-forming, dust temperatures drop considerably (sample-averaged $T_d' = 37 \pm 3$ K), while the mean dust mass is essentially unchanged, $M_d' = (1.6 \pm 0.5) \times 10^7 M_\odot$. No major

differences are found in terms of the dust radius and SN yield. We confirm a compact, but slightly more extended configuration in which $r_d < 0.69$ kpc (REBELS-27 having the largest radius) in all galaxies. We find $0.14 \leq y_d/M_\odot \leq 0.57$, with mean value $\langle y_d \rangle = 0.29 M_\odot$, i.e. about a factor 3 below the MW value. In this case the need for dust growth in the ISM is sensibly decreased.

3.2.2. *Spherical geometry*

The differences between the slab and spherical geometries are minor. Although in this geometry galaxies are more transparent, as inferred by comparing τ_{1500} values in Tab. 3, all other quantities are virtually the same as in the slab case, with gaps amounting to a few percent. These are even smaller than for MW, for which the larger opacities amplify the differences induced by geometry. This configuration allows solutions only for 3 galaxies, and therefore its statistical significance is rather weak.

3.3. *General trends*

To conclude the analysis of the model, we discuss the general trends among the various derived physical quantities. As they are similar in the MW and SMC cases, we quantitatively refer for brevity only to the MW one. The corner plot in Fig. 4 provides a bird's eye view of the trends discussed here. A few noticeable relations are worth highlighting.

The transparency of galaxies, quantified by T_{1500}, increases with r_d and dust mass, but it decreases with dust temperature, and SFR. As in compact configurations the dust column is larger, more UV gets absorbed (decreasing T_{1500}), leading to more efficient dust heating, and hence higher dust temperatures.

While M'_d does not depend strongly on SFR, actively star-forming systems have higher dust temperatures, and consequently $L_{\rm IR}$. In fact, $L_{\rm IR}$ seems to correlate very well with T'_d and anti-correlate with dust mass. In turn, higher dust temperatures are found in more compact, less dusty systems for which the SFR per unit area is larger.

To summarise we can broadly divide the galaxies in the sample (at least those for which our model yields a solution; for a discussion on the remaining systems see Sec. 5) in two classes. In reality, the galaxy properties fall along a continuum sequence (see Fig. 4); however, the differences at the extremes justify the introduction of such rough separation.

The first class (Class I) contains galaxies that are compact, and have large SFR (hence, particularly high $\Sigma_{\rm SFR} \gtrsim 300\,M_\odot {\rm kpc}^{-2}$), and low I_m values. They are opaque, and have large IR luminosities; their dust is

warm but present in limited amounts. The prototypical example of Class I is REBELS-18. The second class (Class II) contains systems that are more extended, moderately star forming and transparent, have a low $\Sigma_{\rm SFR} \lesssim 300 M_\odot {\rm kpc}^{-2}$ and large I_m values. As a result their $L_{\rm IR}$ is about 4 times smaller than the corresponding Class I objects. Dust in these galaxies is cooler but more abundant. A representative object of Class II is REBELS-14. Whether such scenario corresponds to an evolutionary sequence remains to be ascertained. A precise determination of the stellar mass and age is therefore crucial to either support or discard this hypothesis.

4. ADDITIONAL IMPLICATIONS

In the following we explore additional implications of our results by using empirical data not included in the model so far. These are the [CII] 158μm line-SFR relation, and the deviation from the Kennicutt-Schmidt relation, i.e. the burstiness of the REBELS galaxies.

4.1. *[CII] line luminosity – SFR relation*

For many targets, along with the $\approx 158\mu$m dust continuum, the REBELS survey has also measured the [CII] 158μm line flux. There are indications that high-z galaxies align on a well-defined relation between the line luminosity, $L_{\rm CII}$, and SFR (e.g. Carniani et al. 2018, 2020). This relation was first discovered locally (De Looze et al. 2014), but it has recently firmly confirmed for 118 galaxies at $4.4 < z < 5.9$ by the ALPINE collaboration (Schaerer et al. 2020). The original fit for starburst galaxies suggested by De Looze et al. (2014) is given by

$$\log L_{\rm CII} = 7.06 \pm 0.33 + (1.0 \pm 0.04) \log {\rm SFR}; \quad (20)$$

here we adopt this relation, but note that Carniani et al. (2020) find a slightly larger zero-point 1σ dispersion of ± 0.48 dex. According to these authors, such larger dispersion may be associated with the presence of kpc-scale sub-components that are not common in the local Universe.

For completeness we show in Fig. 5 also the ALPINE relation given in Schaerer et al. (2020, Tab. A1):

$$\log L_{\rm CII} = 7.03 \pm 0.17 + (1.0 \pm 0.12) \log {\rm SFR}. \quad (21)$$

We warn that such fit has been obtained with assumptions that are different from the ones adopted here: they use a SMC-like extinction curve and a fixed dust temperature $T_d = 45$ K. Hence, the comparison with the ALPINE data is not fully consistent.

As our model predicts the total SFR of a galaxy, we can use the measured $L_{\rm CII}$ to verify whether the

Table 3. Measured and model-predicted REBELS galaxy properties for a SMC extinction curve and different geometries.

								SLAB GEOMETRY						
	Measured			ID#				*Derived*						
β	F_{1500}	F_{158}	M_*		τ_{1500}	T_{1500}	SFR	$L_{\rm IR}$	T'_d	M'_d	r_d	y_d	κ_s
	μJy	μJy	$M_\odot$				$M_\odot$ yr^{-1}	$L_\odot$	K	$M_\odot$	kpc	$M_\odot$	
-1.29	0.315	67.2	1.45e+09	REBELS-05	2.586	0.436	20.5	1.36e+11	36.9	1.55e+07	0.445	0.57	1.4
-1.24	0.329	76.7	3.16e+09	REBELS-06	2.712	0.420	23.7	1.61e+11	36.4	2.04e+07	0.504	0.34	1.2
-2.17	0.363	101.4	1.05e+09	REBELS-08	...	...	...	...	...	...	...	...	...
-1.99	0.543	86.8	8.71e+08	REBELS-12	...	...	...	...	...	...	...	...	...
-2.21	0.704	60.0	5.37e+08	REBELS-14	...	...	...	...	...	...	...	...	...
-1.34	0.448	52.9	3.09e+09	REBELS-18	2.461	0.453	35.6	2.29e+11	42.3	1.14e+07	0.387	0.20	3.3
-2.33	0.242	71.2	6.17e+08	REBELS-19	...	...	...	...	...	...	...	...	...
-1.85	0.263	259.5	7.76e+09	REBELS-25	...	...	...	...	...	...	...	...	...
-1.79	0.359	50.6	4.90e+09	REBELS-27	1.379	0.632	18.2	7.88e+10	31.8	2.44e+07	0.687	0.26	0.9
-1.61	0.547	56.1	4.17e+09	REBELS-29	1.803	0.553	29.2	1.53e+11	39.9	1.09e+07	0.416	0.14	3.0
-1.50	0.313	60.4	3.55e+09	REBELS-32	2.068	0.510	18.3	1.05e+11	34.4	1.89e+07	0.524	0.28	1.0
-2.18	0.404	163.0	3.80e+09	REBELS-38	...	...	...	...	...	...	...	...	...
-1.96	0.797	79.7	3.63e+08	REBELS-39	...	...	...	...	...	...	...	...	...
-1.44	0.302	48.3	3.02e+09	REBELS-40	2.215	0.488	21.1	1.27e+11	37.1	1.44e+07	0.447	0.25	1.6
				SPHERICAL GEOMETRY									
	Measured			ID#				*Derived*						
β	F_{1500}	F_{158}	M_*		τ_{1500}	T_{1500}	SFR	$L_{\rm IR}$	T'_d	M'_d	r_d	y_d	κ_s
	μJy	μJy	$M_\odot$				$M_\odot$ yr^{-1}	$L_\odot$	K	$M_\odot$	kpc	$M_\odot$	
-1.29	0.315	67.2	1.45e+09	REBELS-05	1.324	0.437	20.5	1.35e+11	36.9	1.56e+07	0.512	0.57	1.5
-1.24	0.329	76.7	3.16e+09	REBELS-06	1.381	0.421	23.7	1.61e+11	36.3	2.05e+07	0.578	0.34	1.3
-2.17	0.363	101.4	1.05e+09	REBELS-08	...	...	...	...	...	...	...	...	...
-1.99	0.543	86.8	8.71e+08	REBELS-12	...	...	...	...	...	...	...	...	...
-2.21	0.704	60.0	5.37e+08	REBELS-14	...	...	...	...	...	...	...	...	...
-1.34	0.448	52.9	3.09e+09	REBELS-18	...	...	...	...	...	...	...	...	...
-2.33	0.242	71.2	6.17e+08	REBELS-19	...	...	...	...	...	...	...	...	...
-1.85	0.263	259.5	7.76e+09	REBELS-25	...	...	...	...	...	...	...	...	...
-1.79	0.359	50.6	4.90e+09	REBELS-27	...	...	...	...	...	...	...	...	...
-1.61	0.547	56.1	4.17e+09	REBELS-29	0.957	0.554	29.2	1.53e+11	39.8	1.09e+07	0.491	0.14	3.5
-1.50	0.313	60.4	3.55e+09	REBELS-32	...	...	...	...	...	...	...	...	...
-2.18	0.404	163.0	3.80e+09	REBELS-38	...	...	...	...	...	...	...	...	...
-1.96	0.797	79.7	3.63e+08	REBELS-39	...	...	...	...	...	...	...	...	...
-1.44	0.302	48.3	3.02e+09	REBELS-40	...	...	...	...	...	...	...	...	...

NOTE—F_{158} fluxes are uncorrected for CMB effects. $L_{\rm IR}$ is computed from UV properties using eq. 13; it therefore might differ from the value obtained by Inami et al. 2021, in prep. which uses a different method.

REBELS galaxies follow the same trend also at their mean $z \approx 7$. Among the 14 galaxies listed in Tab. 1, 13 have also a [CII] line measurement (REBELS-06 is undetected, see footnote 4). We can then associate the predicted SFR to the measured $L_{\rm CII}$ for each of them and compare it with the relation in eq. 20. The relation is shown in Fig. 5 along with the model (SFR) and data ($L_{\rm CII}$) points for the 13 REBELS galaxies. They are cal-

culated for MW (Tab. 2) and SMC (Tab. 3) extinction curves in the slab geometry case.

The 9 REBELS galaxies with a solution and a [CII] detection nicely follow the local starburst galaxies relation if a MW extinction curve is adopted. This is far from trivial because the model does not use the [CII] line information at all. Moreover, this result strengthens the basis of the new method (Sommovigo et al. 2021)
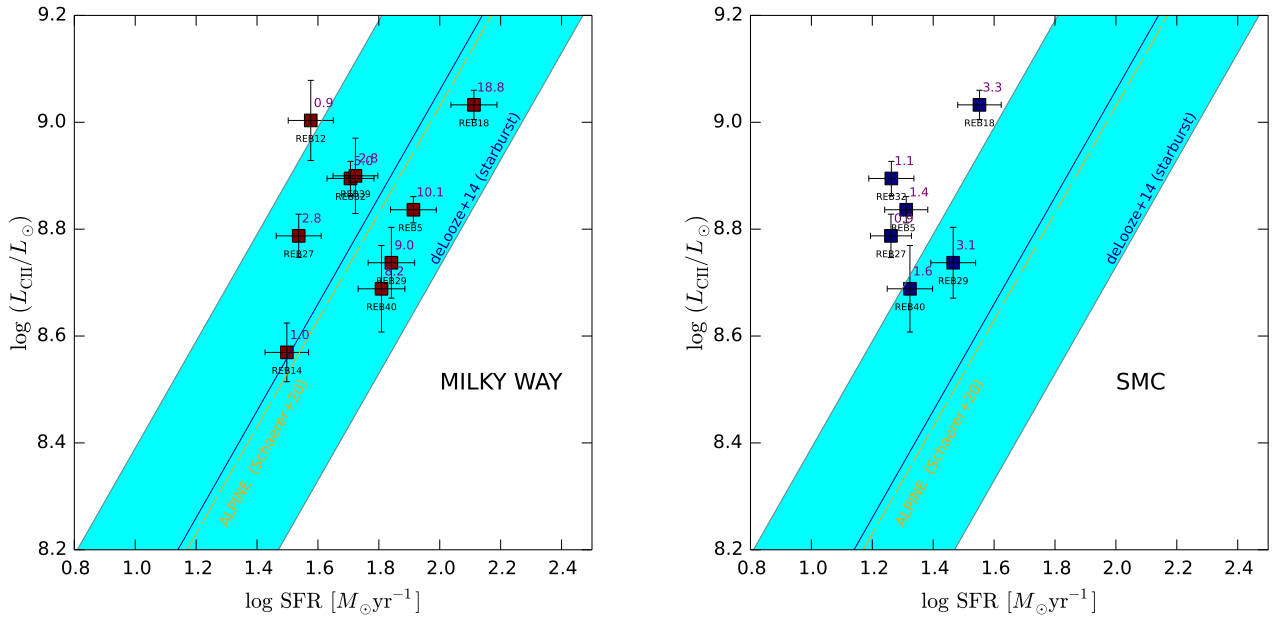
Figure 5. *Left panel:* [CII] luminosity as a function of the predicted SFR for 9 REBELS galaxies (red points) for a MW extinction curve and slab geometry; the L_{CII} values and errors are measured by the REBELS survey. Among the 10 galaxies with a solution, REBELS-06 is undetected in [CII] and therefore does not appear in the plot. The REBELS galaxies ($z \approx 7$) closely follow the local starburst relation (De Looze et al. 2014, aqua band). Also shown for completeness is the ALPINE (Schaerer et al. 2020, orange dashed) relation for $4.4 < z < 5.9$ galaxies. For each galaxy we give the corresponding burstiness parameter, κ_s, value (purple) quantifying the upward deviation from the Kennicutt-Schmidt relation (eq. 22 with $y_P = 2$) *Right:* Same as left panel, for a SMC curve and slab geometry. In this case the REBELS galaxies appear to be off and above the relation.

to infer the dust temperature combining [CII] line and continuum luminosity. Such method is in fact based on the assumption that eq. 20 holds also in the EoR.

For a SMC curve, instead, all REBELS galaxies lie considerably off and above the relation. Note that in general high-z galaxies tend to lie *below* the relation[16]. We consider this as an indication that galaxies in the REBELS sample might preferentially have a MW-like extinction curve.

4.2. *Burstiness & gas depletion time*

Using the model results, we can also investigate whether REBELS galaxies are starbursting. To quantify this statement we follow Ferrara et al. (2019) and introduce the "burstiness" parameter κ_s, accounting for upward deviations from the Kennicutt-Schmidt (KS) average relation[17] (e.g. Heiderman et al. 2010):

$$\Sigma_{SFR} = 10^{-12} \kappa_s \Sigma_g^m \qquad (m = 1.4). \qquad (22)$$

---

[16] See discussion in Ferrara et al. (2019) and Carniani et al. (2018).

[17] The star formation rate (gas mass) per unit area, Σ_{SFR}, (Σ_g) is expressed in units of $M_\odot$ yr^{-1} kpc^{-2} ($M_\odot$ kpc^{-2}).

Galaxies with $\kappa_s > 1$ show a larger SFR per unit area with respect to those located on the KS relation having the same value of Σ_g, i.e. they tend to be starburst. Values of up to $\kappa_s = 100$ have been measured for sub-millimeter galaxies, e.g. Hodge et al. (2015); Vallini et al. (2021).

To compute κ_s from eq. 22 we need two additional quantities: (a) the radius of the stellar, r_*, and gas, r_g, distribution; (b) the gas mass, M_g. For the former, we assume $r_g = y_P r_* = y_P r_d$ where y_P, referred to as the Perito ratio after Carniani et al. (2018), is a factor $\gtrsim 1$. The previous equalities are inspired by the empirical evidence that in high-z galaxies, the gas (traced by [CII] emission) is more extended than the dust/stellar emitting regions which instead show a similar size (Fujimoto et al. 2019, 2020; Carniani et al. 2020; Ginolfi et al. 2020). These studies suggest that $y_P \approx 2$; we adopt this value here, but note that the κ_s values shown in Fig. 5 can be easily scaled to other y_P choices recalling that, from eq. 22 and the relation $r_g = y_P r_*$, $\kappa_s \propto y_P^{2m} = y_P^{2.8}$. We then use r_* and r_g to write $\Sigma_{SFR} = SFR/\pi r_*^2$, and $\Sigma_g = M_g/\pi r_g^2$. This leads us to the final step, i.e. the determination of the gas mass which is deduced from

the predicted dust mass: $M_g = M'_d/D$, where D is the dust-to-gas ratio[18] for $Z = 0.004$.

The derived κ_s values are shown in Fig. 5 by the numbers close to each galaxy point, and reported in Tab. 2 and Tab. 3 for all cases. For the MW we find $0.9 < \kappa_s < 18.8$, with most actively star forming systems showing larger deviations from the KS relation (i.e. they have larger κ_s values). On this basis, we conclude that REBELS galaxies, in addition to the L_{CII}-SFR relation, approximately follow the KS one as well, although a few appear to be relatively bursty (as e.g. REBELS-18, $\kappa_s = 18.8$). This conclusion holds also for the SMC extinction curve: in fact, we find $0.9 < \kappa_s < 3.3$.

Finally, we can compute the mean gas depletion timescale, t_d, for the sample,

$$t_{dep} = \frac{\Sigma_g}{\Sigma_{SFR}} = \frac{M'_d}{D\,SFR} y_P^{-2} = 0.11\, y_P^{-2}\,\mathrm{Gyr}, \qquad (23)$$

having assumed SFR $= 65.8\,\mathrm{M_\odot yr^{-1}}$ and $M'_d = 1.3 \times 10^7 M_\odot$ as the mean values for the MW/slab configuration. This result can be compared with the extrapolation of the $z < 4$ relation found by Tacconi et al. (2018) from the PHIBBS survey for galaxies located on the main sequence[19]

$$\log(t_{dep}/\mathrm{Gyr}) = 0.09 - 0.62\log(1 + z). \qquad (24)$$

When evaluated at the REBELS sample mean redshift, $\langle z_s \rangle = 7.01$, eq. 24 gives $t_{dep} = 0.34$ Gyr, formally requiring a Perito ratio $y_P = 0.57$. As such value is somewhat in tension with [CII] observations indicating $y_P \approx 2$, this result might indicate that the extrapolation of the PHIBBS relation into the EoR results in an overestimate of the depletion time. Further work is necessary to clarify this issue in detail.

5. WHERE THE IRX RELATION FAILS

At the beginning of Sec. 3 we have noted that a solution cannot be found with our method for some galaxies both for MW and SMC extinction curve cases, and we provided there a first qualitative explanation. Here we additionally note that such no-solution cases are characterized by large I_m values. In other words, these peculiar galaxies have a very large IR-to-UV flux ratio compared

---

[18] We assume that $D \propto Z$. Then for the MW $D_{MW} = 1/162$ (Rémy-Ruyer et al. 2014), $Z = 0.004$ implies $D = 1/575$. For completeness, the value for the SMC is $D_{SMC} = 1/1408$.

[19] Of course, there is no guarantee that REBELS galaxies are located on such relation. In addition, strictly speaking, the depletion time in the PHIBBS sample is computed for molecular, rather than total gas mass. By using this formula we implicitly assume that $M_{H2} \approx M_g$, which for such high-z galaxies should represent a reasonable approximation (Tacconi et al. 2018).

REBELS-19 (UVISTA-Y-879)
JHK-band image
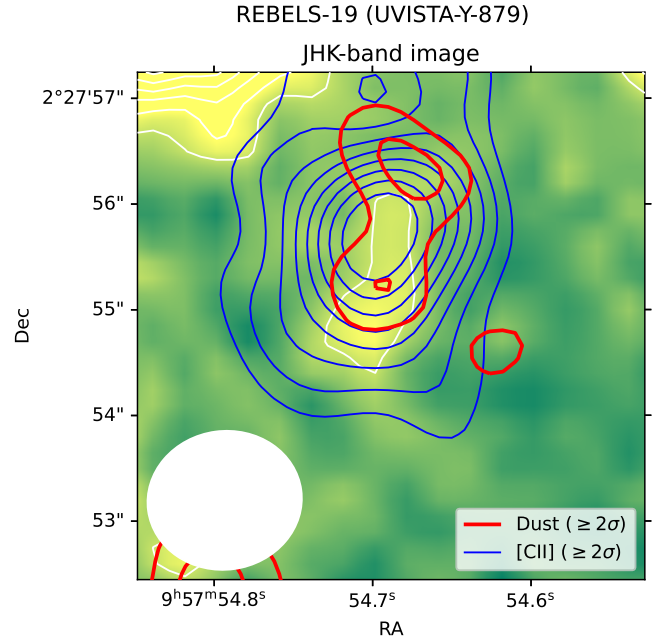
Figure 6. FIR 158μm dust continuum (red) and [CII] line (blue) emission contours for REBELS-19 ($z = 7.37$) superposed to the JHK-band composite image and (white) contours. The contours start from 2σ and increase in steps of 1σ. The white ellipse at the bottom left shows the beam size; thin dotted line contours indicate negative sources. The spatial segregation between the FIR and the restframe UV emission is evident. For more details see Inami et al. 2021, in prep.

to their UV slope. Let us see how this can be understood.

Using the depletion time definition in eq. 23 one can write an approximate expression for the SED "color", i.e. the F_{158}/F_{1500} ratio, predicted by the model by combining eq. 18 and 12:

$$\frac{F_{158}}{F_{1500}} \simeq 7062\frac{y}{T_{1500}} \exp\left[-3\left(\frac{y}{1 - T_{1500}}\right)^{1/6}\right], \quad (25)$$

where $y = (Z/Z_\odot)(t_{dep}/\mathrm{Gyr})$. Such expression is valid in the temperature range $T_{CMB} \lesssim T_d \lesssim T_{158} = h_P\nu_{158}/k_B = 91.2$ K, as we have neglected the presence of the CMB in eq. 18. Eq. 25 entails interesting physical implications. For a given T_{1500} value, galaxies with a longer depletion time (recall that in this paper we have fixed $Z = 0.28Z_\odot$) have redder SED colors. Alternatively, for a given t_{dep}, the ratio increases towards more opaque (lower T_{1500}) systems.

Let us now divide the above flux ratio by $(\beta - \beta_{int}) = -\ln T_{1500} = \tau_{eff}$, to obtain the quantity we have defined as the molecular index, I_m in eq. 3, and take the optically thin limit, for which $1 - T_{1500} \approx \tau_{eff}$ and $T_{1500} \approx 1$.

Then,

$$I_{\mathrm{m}} = \frac{(F_{158}/F_{1500})}{(\beta - \beta_{\mathrm{int}})} \simeq 7062 \; x e^{-3x^{1/6}}, \qquad (26)$$

where $x = y/\tau_{\mathrm{eff}}$. The previous expression has a maximum located at $x_{\mathrm{max}} = 64$, corresponding to $I_m^* \equiv I_m(x_{\mathrm{max}}) \simeq 1120$ (for the MW). Hence, galaxies showing values of $I_m > I_m^*$ cannot be reproduced by a single zone model. Physically, this depends on the fact that F_{158} can be increased by raising the dust mass or the temperature. However, increasing M_d' while keeping $(\beta - \beta_{\mathrm{int}})$ (i.e. the effective optical depth) low[20] implies pushing the dust temperatures to values progressively closer to the CMB, thus preventing F_{158}, and hence I_m, to increase beyond I_m^*. These findings are confirmed by the results reported in the Tables. Indeed, for the MW case, the no-solution galaxies all have $I_m > 1183$.

We conclude that $I_m > I_m^*$ values can be achieved only if the FIR luminosity is spatially decoupled from the UV emitting regions. In such a scenario, the former is produced in optically thick, star forming clumps (likely, giant molecular complexes), and produce the high F_{158} values required. The small UV optical depth is produced instead by the diffuse, interclump gas component in which young stars are embedded after they disperse their natal cloud. This two-phase configuration should then characterise no-solution galaxies.

We speculate that no-solution galaxies are extreme Class II systems, as defined in Sec. 3.3, which have developed a prominent two-phase ISM structure with spatially segregated IR and UV emitting regions throughout their disk. This hypothesis is supported by Fig. 6, showing the continuum and [CII] emission, along with the restframe UV image of REBELS-19, a no-solution case. The spatial displacement between the continuum and UV emission is clearly visible. Once observed at higher spatial resolution, other REBELS no-solution galaxies might show a similar spatially decoupled structure. As a final caveat, we note that the above scenario questions the use of the IRX-β relation, which implicitly assumes that the IR and UV emission are co-spatial. According to our results such relation can be only safely applied to galaxies with $I_m \lesssim I_m^*$

6. SUMMARY

We have analyzed the FIR dust continuum measurements obtained for 14 $z \approx 7$ galaxies by the ALMA REBELS Large Program, in combination with rest-frame UV data, with the aim of deriving the physical properties of these early systems. Our method uses as a input three measurements, i.e. (a) the UV spectral slope, β, (b) the observed UV continuum flux, F_{1500} at 1500Å, (c) the observed far-infrared continuum flux, F_{158}, at $\approx 158\mu$m to derive 7 quantities (τ_{1500}, T_{1500}, SFR, L_{IR}, T_d', M_d', r_d). An additional one, the dust yield per supernova, y_d, is obtained using external information on the galaxy stellar mass.

The results are summarized in Tab. 2 and Tab. 3 for the MW and SMC curves, respectively, and for different dust/stellar relative geometries. They are also graphically shown in Fig. 4. In general, we find that different geometries have little impact on the parameter determination; changing the extinction curve has instead a significant impact. For example, the estimated SFR is $\approx 3\times$ lower for a SMC curve. We argue in Sec. 4 that on the basis of the measured [CII] line luminosity, the MW extinction curve appears to be preferable.

The key results for the fiducial (MW extinction case) are summarized as follows.

- ■ REBELS galaxies are *physically* optically thick at 1500Å but due to geometrical radiative transfer effects they are relatively transparent (i.e. low *effective* optical depth, see Sec. 2.1), with $28 - 90.5\%$ of the star formation being obscured[21]. The total star formation rates are in the range $31.5 < \mathrm{SFR}/(\mathrm{M_\odot yr^{-1}}) < 129.5$ with REBELS-14 (REBELS-18) being the least (most) star forming system.

- ■ The sample-averaged dust mass and temperature are $(1.3 \pm 1.1) \times 10^7 M_\odot$ and 52 ± 11 K, respectively. However, in some galaxies dust is particularly abundant (REBELS-14, $M_d' \approx 3.4 \times 10^7 M_\odot$), or hot (REBELS-18, $T_d' \approx 67$ K). The dust distribution is compact with 70% of the galaxies showing $r_d < 0.3$ kpc. Such compact configuration, in general, produces high dust temperatures: the hottest REBELS-18 indeed is the most compact system with $r_d = 0.16$ kpc.

- ■ By augmenting the method with stellar mass information obtained by the REBELS Collaboration from SED fitting, we estimate the dust yield per supernova, y_d. We find that $0.1 \leq y_d/M_\odot \leq 3.3$, with 70% of the galaxies requiring $y_d < 0.25 M_\odot$.

---

[20] Recall that β_{int} in our model is computed (Sec. 2) self-consistently with IMF, age, metallicity, Z and $\mathcal{K}_{1500}$; therefore, it cannot be varied independently.

[21] We prefer to define these galaxies as "relatively transparent" as (i) they are all detected in UV, and (b) because their V-band optical depth is $\lesssim 3$, i.e. it is not extremely high as for obscured, sub-millimeter galaxies.

Three galaxies (REBELS-12, 14, 39) require $y_d > 1 M_\odot$, which is likely inconsistent with pure SN production, and might require dust growth via accretion of heavy elements from the ISM. We warn that using non-parametric star formation histories might increase the stellar masses by ≈ 3 times, thus reducing the above yields by the same factor.

■ With the SFR predicted by the model, REBELS galaxies detected in [CII] nicely follow the local $L_{\rm CII}-$SFR relation (De Looze et al. 2014) if a MW extinction curve is adopted. For a SMC curve, instead, all REBELS galaxies lie considerably off and above the relation. We also show that REBELS galaxies are approximately located on the Kennicutt-Schmidt relation (burstiness parameter $k_s \lesssim 18.8$). The sample-averaged gas depletion time is of $0.11 \, y_P^{-2}$ Gyr, where y_P is the ratio of the gas-to-stellar distribution radius.

■ For some systems (4 in the case of the MW curve) a solution simultaneously matching the observed $(\beta, F_{1500}, F_{158})$ values cannot be found. This occurs when the molecular index $I_m = F_{158}/F_{1500}(\beta - \beta_{\rm int})$ exceeds the threshold $I_m^* \approx 1120$ for a MW extinction curve. For these objects (REBELS-19 being the most outstanding example) we argue that the FIR luminosity is not co-spatial with the UV-emitting regions, questioning the use of the IRX-β relation.

Data Availability

Data available on request.

REFERENCES

Arata, S., Yajima, H., Nagamine, K., Li, Y., & Khochfar, S. 2019, MNRAS, 488, 2629, doi: 10.1093/mnras/stz1887

Asplund, M., Grevesse, N., Sauval, A. J., & Scott, P. 2009, Annual Review of Astronomy and Astrophysics, 47, 481–522, doi: 10.1146/annurev.astro.46.060407.145222

Baes, M., & Dejonghe, H. 2001, MNRAS, 326, 733, doi: 10.1046/j.1365-8711.2001.04626.x

Bakx, T. J. L. C., Tamura, Y., Hashimoto, T., et al. 2020, MNRAS, 493, 4294, doi: 10.1093/mnras/staa509

Bakx, T. J. L. C., Sommovigo, L., Carniani, S., et al. 2021, MNRAS, 508, L58, doi: 10.1093/mnrasl/slab104

Behrens, C., Pallottini, A., Ferrara, A., Gallerani, S., & Vallini, L. 2018, MNRAS, 477, 552, doi: 10.1093/mnras/sty552

Bethermin, M., Fudamoto, Y., Ginolfi, M., et al. 2020, arXiv e-prints, arXiv:2002.00962. https://arxiv.org/abs/2002.00962

Bhatawdekar, R., & Conselice, C. J. 2021, ApJ, 909, 144, doi: 10.3847/1538-4357/abdd3f

Bouwens, R. J., Illingworth, G. D., Oesch, P. A., et al. 2014, ApJ, 793, 115, doi: 10.1088/0004-637X/793/2/115

Bouwens, R. J., Oesch, P. A., Labbé, I., et al. 2016, ApJ, 830, 67, doi: 10.3847/0004-637X/830/2/67

Bouwens, R. J., Oesch, P. A., Stefanon, M., et al. 2021a, arXiv e-prints, arXiv:2102.07775. https://arxiv.org/abs/2102.07775

Bouwens, R. J., Smit, R., Schouws, S., et al. 2021b, arXiv e-prints, arXiv:2106.13719. https://arxiv.org/abs/2106.13719

Bowler, R. A. A., Jarvis, M. J., Dunlop, J. S., et al. 2020, MNRAS, 493, 2059, doi: 10.1093/mnras/staa313

Bowler, R. A. A., Dunlop, J. S., McLure, R. J., et al. 2015, MNRAS, 452, 1817, doi: 10.1093/mnras/stv1403

Calzetti, D. 2001, PASP, 113, 1449, doi: 10.1086/324269

Carniani, S., Maiolino, R., Amorin, R., et al. 2018, MNRAS, 478, 1170, doi: 10.1093/mnras/sty1088

Carniani, S., Ferrara, A., Maiolino, R., et al. 2020, MNRAS, 499, 5136, doi: 10.1093/mnras/staa3178

Casey, C. M., Narayanan, D., & Cooray, A. 2014, Physics Reports, 541, 45, doi: https://doi.org/10.1016/j.physrep.2014.02.009

Cherchneff, I. 2014, arXiv e-prints, arXiv:1405.1216. https://arxiv.org/abs/1405.1216

Chevallard, J., & Charlot, S. 2016, MNRAS, 462, 1415, doi: 10.1093/mnras/stw1756

Choudhury, S., Subramaniam, A., Cole, A. A., & Sohn, Y.-J. 2018, Monthly Notices of the Royal Astronomical Society, 475, 4279–4297, doi: 10.1093/mnras/sty087

Choudhury, T. R., Ferrara, A., & Gallerani, S. 2008, MNRAS, 385, L58, doi: 10.1111/j.1745-3933.2008.00433.x

Ciardi, B., & Ferrara, A. 2005, SSRv, 116, 625, doi: 10.1007/s11214-005-3592-0

Code, A. D. 1973, in Interstellar Dust and Related Topics, ed. J. M. Greenberg & H. C. van de Hulst, Vol. 52, 505

Cormier, D., Abel, N. P., Hony, S., et al. 2019, A&A, 626, A23, doi: 10.1051/0004-6361/201834457

Cortese, L., Boselli, A., Buat, V., et al. 2006, ApJ, 637, 242, doi: 10.1086/498296

Da Cunha, E., Groves, B., Walter, F., et al. 2013, The Astrophysical Journal, 766, 13

Dayal, P., & Ferrara, A. 2012, MNRAS, 421, 2568, doi: 10.1111/j.1365-2966.2012.20486.x

—. 2018, PhR, 780, 1, doi: 10.1016/j.physrep.2018.10.002

De Looze, I., Cormier, D., Lebouteiller, V., et al. 2014, A&A, 568, A62, doi: 10.1051/0004-6361/201322489

Di Mascia, F., Gallerani, S., Ferrara, A., et al. 2021a, MNRAS, 506, 3946, doi: 10.1093/mnras/stab1876

Di Mascia, F., Gallerani, S., Behrens, C., et al. 2021b, MNRAS, 503, 2349, doi: 10.1093/mnras/stab528

Draine, B. T. 2003, ARA&A, 41, 241, doi: 10.1146/annurev.astro.41.011802.094840

Dudzevičiūtė, U., Smail, I., Swinbank, A. M., et al. 2020, MNRAS, 494, 3828, doi: 10.1093/mnras/staa769

Dunlop, J. S. 2013, Observing the First Galaxies, ed. T. Wiklind, B. Mobasher, & V. Bromm, Vol. 396, 223, doi: 10.1007/978-3-642-32362-1_5

Faisst, A. L., Fudamoto, Y., Oesch, P. A., et al. 2020, arXiv e-prints, arXiv:2005.07716. https://arxiv.org/abs/2005.07716

Ferrara, A., Bianchi, S., Cimatti, A., & Giovanardi, C. 1999, ApJS, 123, 437, doi: 10.1086/313244

Ferrara, A., & Peroux, C. 2021, MNRAS, 503, 4537, doi: 10.1093/mnras/stab761

Ferrara, A., Vallini, L., Pallottini, A., et al. 2019, MNRAS, 489, 1, doi: 10.1093/mnras/stz2031

Ferrara, A., Viti, S., & Ceccarelli, C. 2016, MNRAS, 463, L112, doi: 10.1093/mnrasl/slw165

Fixsen, D. J. 2009, ApJ, 707, 916, doi: 10.1088/0004-637X/707/2/916

Fudamoto, Y., Oesch, P. A., Schouws, S., et al. 2021, Nature, 597, 489–492, doi: 10.1038/s41586-021-03846-z

Fujimoto, S., Ouchi, M., Ferrara, A., et al. 2019, ApJ, 887, 107, doi: 10.3847/1538-4357/ab480f

Fujimoto, S., Silverman, J. D., Bethermin, M., et al. 2020, ApJ, 900, 1, doi: 10.3847/1538-4357/ab94b3

Gall, C., & Hjorth, J. 2018, ApJ, 868, 62, doi: 10.3847/1538-4357/aae520

Galliano, F., Galametz, M., & Jones, A. P. 2018, ARA&A, 56, 673, doi: 10.1146/annurev-astro-081817-051900

Ginolfi, M., Graziani, L., Schneider, R., et al. 2018, MNRAS, 473, 4538, doi: 10.1093/mnras/stx2572

Ginolfi, M., Jones, G. C., Béthermin, M., et al. 2020, A&A, 633, A90, doi: 10.1051/0004-6361/201936872

Graziani, L., Schneider, R., Ginolfi, M., et al. 2020, MNRAS, 494, 1071, doi: 10.1093/mnras/staa796

Gruppioni, C., Béthermin, M., Loiacono, F., et al. 2020, A&A, 643, A8, doi: 10.1051/0004-6361/202038487

Hashimoto, T., Inoue, A. K., Mawatari, K., et al. 2019, PASJ, 71, 71, doi: 10.1093/pasj/psz049

Heiderman, A., Evans, II, N. J., Allen, L. E., Huard, T., & Heyer, M. 2010, ApJ, 723, 1019, doi: 10.1088/0004-637X/723/2/1019

Hirashita, H., Ferrara, A., Dayal, P., & Ouchi, M. 2015, in Astronomical Society of the Pacific Conference Series, Vol. 499, Revolution in Astronomy with ALMA: The Third Year, ed. D. Iono, K. Tatematsu, A. Wootten, & L. Testi, 67

Hodge, J. A., & da Cunha, E. 2020, Royal Society Open Science, 7, 200556, doi: 10.1098/rsos.200556

Hodge, J. A., Riechers, D., Decarli, R., et al. 2015, ApJ, 798, L18, doi: 10.1088/2041-8205/798/1/L18

Hunter, J. D. 2007, Computing in Science and Engineering, 9, 90, doi: 10.1109/MCSE.2007.55

Inoue, A. K., Hashimoto, T., Chihara, H., & Koike, C. 2020, MNRAS, 495, 1577, doi: 10.1093/mnras/staa1203

Ishigaki, M., Kawamata, R., Ouchi, M., et al. 2018, ApJ, 854, 73, doi: 10.3847/1538-4357/aaa544

Jones, G. C., Willott, C. J., Carilli, C. L., et al. 2017, ApJ, 845, 175, doi: 10.3847/1538-4357/aa7d0d

Kennicutt, Robert C., J. 1998, ARA&A, 36, 189, doi: 10.1146/annurev.astro.36.1.189

Kohandel, M., Pallottini, A., Ferrara, A., et al. 2020, MNRAS, 499, 1250, doi: 10.1093/mnras/staa2792

—. 2019, MNRAS, 487, 3007, doi: 10.1093/mnras/stz1486

Krügel, E. 2009, A&A, 493, 385, doi: 10.1051/0004-6361:200809976

Laporte, N., Ellis, R. S., Boone, F., et al. 2017, ApJL, 837, L21, doi: 10.3847/2041-8213/aa62aa

Leitherer, C., Schaerer, D., Goldader, J. D., et al. 1999, ApJS, 123, 3, doi: 10.1086/313233

Leśniewska, A., & Michałowski, M. J. 2019, A&A, 624, L13, doi: 10.1051/0004-6361/201935149

Liang, L., Feldmann, R., Kereš, D., et al. 2019, MNRAS, 489, 1397, doi: 10.1093/mnras/stz2134

Livermore, R. C., Finkelstein, S. L., & Lotz, J. M. 2017, ApJ, 835, 113, doi: 10.3847/1538-4357/835/2/113

Lotz, J. M., Koekemoer, A., Coe, D., et al. 2017, ApJ, 837, 97, doi: 10.3847/1538-4357/837/1/97

Madau, P., & Dickinson, M. 2014, ARA&A, 52, 415, doi: 10.1146/annurev-astro-081811-125615

Magdis, G. E., Daddi, E., Béthermin, M., et al. 2012, ApJ, 760, 6, doi: 10.1088/0004-637X/760/1/6

Mancini, M., Schneider, R., Graziani, L., et al. 2016, MNRAS, 462, 3130, doi: 10.1093/mnras/stw1783

—. 2015, MNRAS, 451, L70, doi: 10.1093/mnrasl/slv070

Marassi, S., Schneider, R., Limongi, M., et al. 2015, MNRAS, 454, 4250, doi: 10.1093/mnras/stv2267

—. 2019, MNRAS, 484, 2587, doi: 10.1093/mnras/sty3323

McLure, R. J., Dunlop, J. S., Bowler, R. A. A., et al. 2013, MNRAS, 432, 2696, doi: 10.1093/mnras/stt627

Meurer, G. R., Heckman, T. M., & Calzetti, D. 1999, ApJ, 521, 64, doi: 10.1086/307523

Mitra, S., Choudhury, T. R., & Ferrara, A. 2015, MNRAS, 454, L76, doi: 10.1093/mnrasl/slv134

Naidu, R. P., Tacchella, S., Mason, C. A., et al. 2020, ApJ, 892, 109, doi: 10.3847/1538-4357/ab7cc9

Niculescu-Duvaz, M., Barlow, M. J., Bevan, A., Milisavljevic, D., & Looze, I. D. 2021, The dust mass in Cassiopeia A from infrared and optical line flux differences. https://arxiv.org/abs/2103.12705

Oesch, P. A., Bouwens, R. J., Illingworth, G. D., Labbé, I., & Stefanon, M. 2018, ApJ, 855, 105, doi: 10.3847/1538-4357/aab03f

Oesch, P. A., Bouwens, R. J., Carollo, C. M., et al. 2010, ApJL, 725, L150, doi: 10.1088/2041-8205/725/2/L150

Oesch, P. A., Bouwens, R. J., Illingworth, G. D., et al. 2014, ApJ, 786, 108, doi: 10.1088/0004-637X/786/2/108

Ono, Y., Ouchi, M., Harikane, Y., et al. 2018, PASJ, 70, S10, doi: 10.1093/pasj/psx103

Pallottini, A., Ferrara, A., Decataldo, D., et al. 2019, MNRAS, 487, 1689, doi: 10.1093/mnras/stz1383

Pallottini, A., Ferrara, A., Gallerani, S., et al. 2022, arXiv e-prints, arXiv:2201.02636. https://arxiv.org/abs/2201.02636

Popping, G., Somerville, R. S., & Galametz, M. 2017, MNRAS, 471, 3152, doi: 10.1093/mnras/stx1545

Priestley, F. D., Barlow, M. J., & De Looze, I. 2019, MNRAS, 485, 440, doi: 10.1093/mnras/stz414

Rémy-Ruyer, A., Madden, S. C., Galliano, F., et al. 2014, A&A, 563, A31, doi: 10.1051/0004-6361/201322803

Rho, J., Gomez, H. L., Boogert, A., et al. 2018, MNRAS, 479, 5101, doi: 10.1093/mnras/sty1713

Robertson, B. E., Ellis, R. S., Furlanetto, S. R., & Dunlop, J. S. 2015, ApJL, 802, L19, doi: 10.1088/2041-8205/802/2/L19

Salmon, B., Coe, D., Bradley, L., et al. 2018, ApJL, 864, L22, doi: 10.3847/2041-8213/aadc10

Schaerer, D., Ginolfi, M., Béthermin, M., et al. 2020, A&A, 643, A3, doi: 10.1051/0004-6361/202037617

Schouws, S., Stefanon, M., Bouwens, R. J., et al. 2021, arXiv e-prints, arXiv:2105.12133. https://arxiv.org/abs/2105.12133

Schreiber, C., Elbaz, D., Pannella, M., et al. 2018, A&A, 609, A30, doi: 10.1051/0004-6361/201731506

Shen, X., Vogelsberger, M., Nelson, D., et al. 2021, arXiv e-prints, arXiv:2104.12788. https://arxiv.org/abs/2104.12788

Smit, R., Bouwens, R. J., Carniani, S., et al. 2018, Nature, 553, 178, doi: 10.1038/nature24631

Sommovigo, L., Ferrara, A., Carniani, S., et al. 2021, arXiv e-prints, arXiv:2102.08950. https://arxiv.org/abs/2102.08950

Tacconi, L. J., Genzel, R., Saintonge, A., et al. 2018, ApJ, 853, 179, doi: 10.3847/1538-4357/aaa4b4

Temim, T., Dwek, E., Arendt, R. G., et al. 2017, ApJ, 836, 129, doi: 10.3847/1538-4357/836/1/129

Tielens, A. G. G. M. 2010, The Physics and Chemistry of the Interstellar Medium

Todini, P., & Ferrara, A. 2001, MNRAS, 325, 726, doi: 10.1046/j.1365-8711.2001.04486.x

Trebitsch, M., Volonteri, M., & Dubois, Y. 2020, MNRAS, 494, 3453, doi: 10.1093/mnras/staa1012

Vallini, L., Ferrara, A., Pallottini, A., Carniani, S., & Gallerani, S. 2021, MNRAS, 505, 5543, doi: 10.1093/mnras/stab1674

Vogelsberger, M., Nelson, D., Pillepich, A., et al. 2020, MNRAS, 492, 5167, doi: 10.1093/mnras/staa137

Watson, D., Christensen, L., Knudsen, K. K., et al. 2015, Nature, 519, 327, doi: 10.1038/nature14164

Weingartner, J. C., & Draine, B. T. 2001, ApJ, 548, 296, doi: 10.1086/318651

Wilkins, S. M., Feng, Y., Di Matteo, T., et al. 2018, MNRAS, 473, 5363, doi: 10.1093/mnras/stx2588

Wise, J. H. 2019, Contemporary Physics, 60, 145–163, doi: 10.1080/00107514.2019.1631548

APPENDIX

A. DUST TEMPERATURE IN OPTICALLY THICK MEDIA

Consider a uniform absorbing dust layer of total optical depth τ_d, and divide it into N equal slices, each with an optical depth $\Delta\tau = \tau_d/N$. The layer boundary ($N = 0$) is illuminated by an external UV flux, F_0. The flux reaching the i-th slice is $F_i = F_0 \exp(-\tau_i) = F_0 \exp(-i\Delta\tau)$; the absorbed flux is then $F_i(1 - \exp(-\Delta\tau))$. Using eq. 15 for the mean physical temperature (MPT), and specializing for simplicity to the relevant case $\beta_d = 2$, it is easy to show that the dust temperature (assuming that the entire slab is optically thin to re-emitted IR photons) in the i-th slice is

$$T_i = \bar{T}_d \left[N e^{-i\Delta\tau} \frac{(1 - e^{-\Delta\tau})}{(1 - e^{-\tau_d})} \right]^{1/6}. \tag{A1}$$

The temperature therefore decreases with depth into the layer. We therefore define the *mass-weighted* temperature by averaging[22] the non-constant factor over the depth i:

$$\langle e^{-(\tau_d/6N)i} \rangle_M = \frac{1}{N} \int_0^N e^{-(\tau_d/6N)i} di = \frac{6}{\tau_d}(1 - e^{-\tau_d/6}) \tag{A2}$$

Inserting the previous expression in eq. A1,

$$\langle T_i \rangle_M = \bar{T}_d \left[N \frac{(1 - e^{-\tau_d/N})}{(1 - e^{-\tau_d})} \right]^{1/6} \frac{6}{\tau_d}(1 - e^{-\tau_d/6}), \tag{A3}$$

further imposing that all slices are optically thin so that the MPT can be safely applied, $\Delta\tau \ll 1$ or, equivalently, $N \gg 1$, we find

$$\lim_{N\to\infty} \langle T_i \rangle_M = \bar{T}_d \frac{6}{\tau_d^{5/6}} \frac{(1 - e^{-\tau_d/6})}{(1 - e^{-\tau_d})^{1/6}} \equiv \bar{T}_d f_M(\tau_d). \tag{A4}$$

Note that if the layer is optically thin $\tau_d \to 0$, the above formula correctly returns $\langle T_i \rangle_M = \bar{T}_d$. Eq. A4 is shown in Fig. 7. We see that the MPT always overestimates the actual dust temperature, and it is correct only if the layer is optically thin. We note that the actual dust temperature $\langle T_i \rangle$ can be substantially lower than $\bar{T}_d$: for example, if $\tau_d = 8$ (20), $\langle T_i \rangle_M = 0.78\,(0.48)\bar{T}_d$.

More often one wants to use the *luminosity-weighted* temperature, i.e. the temperature of a single-temperature grey-body producing an IR luminosity equal to the absorbed UV luminosity input in the system. This is formally defined as

$$\langle T_i \rangle_L = \frac{\int_0^N T_i F_i di}{\int_0^N F_i di}. \tag{A5}$$

Recalling that $F_i \propto \Theta M_{d,i} T_i^6$, and taking again the limit $N \to \infty$, we find

$$\langle T_i \rangle_L = \bar{T}_d \frac{6}{7} \tau_d^{1/6} \frac{(1 - e^{-7\tau_d/6})}{(1 - e^{-\tau_d})^{7/6}} \equiv \bar{T}_d f_L(\tau_d). \tag{A6}$$

As for the mass-weighted temperature, $\langle T_i \rangle_L = \bar{T}_d$ for optically thin cells. However, the L-weighted temperature *increases* as the cell becomes optically thick. For example, if $\tau_d = 8$ (20), $\langle T_i \rangle_L = 1.2\,(1.4)\bar{T}_d$. Hence, $\langle T_i \rangle_L$ is always larger than $\bar{T}_d$, the cell temperature one would derive by neglecting RT effects. Also, for optically thin cells $\bar{T}_d = \langle T_i \rangle_M = \langle T_i \rangle_L$; however as τ_d increases the mass- and luminosity-weighted temperatures diverge. The ratio between the two temperatures is given by f_L/f_M:

$$\mathcal{R} = \frac{\langle T_i \rangle_L}{\langle T_i \rangle_M} = \frac{f_L}{f_M} = \frac{\tau_d}{7} \frac{1}{(1 - e^{-\tau_d})} \frac{(1 - e^{-7\tau_d/6})}{(1 - e^{-\tau_d})}; \tag{A7}$$

---

[22] As the slices contain the same mass, this averaging is equivalent to a mass averaging
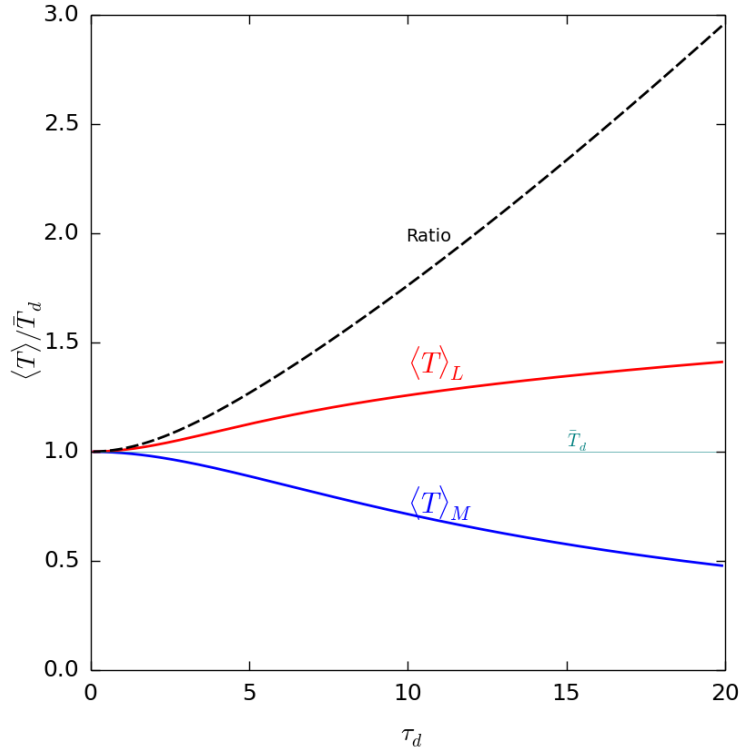
Figure 7. Dependence of the luminosity- and mass-weighted temperatures (for $\beta_d = 2$), along with their ratio, as a function of the total dust optical depth of the layer τ_d in units of the mean physical temperature, $\tilde{T}_d$, defined in eq. 15.

For very optically thick cells, the ratio increases linearly, $\mathcal{R} \simeq \tau_d/7$. It is useful to note that the SED produced by a multi-temperature layer deviates from a single-T graybody: the larger τ_d, the larger is the deviation. Such SED can be *approximated* by a single-T graybody with temperature $T = \langle T_i \rangle_L$ provided that the dust mass is effectively decreased by the ratio $M_d(\bar{T}/\langle T_i \rangle_L)^6 = M_d f_L^{-6}$ so to produce the same total IR luminosity.